# Dynamic fault interaction during a fluid-injection induced earthquake: The 2017 Mw 5.5 Pohang event


- **Kadek Hendrawan Palgunadi[1]** : **kadek.palgunadi@kaust.edu.sa**
- **Alice-Agnes Gabriel[2]** : **gabriel@geophysik.uni-muenchen.de**
- **Thomas Ulrich[2]** : **ulrich@geophysik.uni-muenchen.de**
- **José Ángel Lopéz-Comino[3i]** : **lopezcomino@uni-potsdam.de**
- **Paul Martin Mai[1]** : **martin.mai@kaust.edu.sa**

1. Physical Science and Engineering, King Abdullah University of Science and Technology, Thuwal, Saudi Arabia
2. Department of Earth and Environmental Sciences, Geophysics, Ludwig-Maximilians-Universität München, Theresienstr. 41, 80333 Munich, Germany
3. Institute of Geosciences University of Potsdam, Potsdam-Golm, Germany.




[i]also at Instituto Andaluz de Geofísica, Universidad de Granada, Spain; Departamento de Física Teórica y del Cosmos, Universidad de Granada, Spain; Physical Science and Engineering, King Abdullah University of Science and Technology, Thuwal, Saudi Arabia

**Abstract**:

The November 15th, 2017 Mw 5.5 Pohang earthquake (South Korea) has been linked to hydraulic stimulation and fluid injections, making this the largest induced seismic event associated with an Enhanced Geothermal System (EGS). To understand its source dynamics and fault interactions, we conduct the first 3D high-resolution spontaneous dynamic rupture simulations of an induced earthquake. We account for topography, off-fault plastic deformation under depth-dependent bulk cohesion, rapid velocity weakening friction and 1D subsurface structure. A guided fault reconstruction approach that clusters spatio-temporal aftershock locations (including their uncertainties) is used to identify a main and a secondary fault plane which intersect under a shallow angle of 15°. Based on simple Mohr-Coulomb failure analysis and 180 dynamic rupture experiments in which we vary local stress loading conditions, fluid pressure, and relative fault strength, we identify preferred two fault plane scenarios that well reproduce observations. We find that the regional far-field tectonic stress regime promotes pure strike-slip faulting, while local stress conditions constrained by borehole logging generate the observed thrust faulting component. Our preferred model is characterized by overpressurized pore fluids, non-optimally oriented but dynamically weak faults and a close to critical local stress state. In our model, earthquake rupture "jumps" to the secondary fault by dynamic triggering, generating a measurable non-double couple component. Our simulations suggest that complex dynamic fault interaction may occur during fluid-injection induced earthquakes and that local stress perturbations dominate over the regional stress conditions. These findings, therefore, have important implications for seismic hazard in active geo-reservoir.

# Introduction

The Korean Peninsula is known to have a rather low-level of seismicity (compared to neighboring countries like China and Japan) because it lies on the continental margin of the east Eurasian plate. However, on November 15$^{th}$, 2017 (05:29:31 UTC), a magnitude Mw 5.5 earthquake occurred (hereinafter the Pohang earthquake), the second-largest recorded earthquake in South Korea following the 2016 Mw 5.5 Gyeongju earthquake. The Pohang earthquake caused one fatality, injured 82 people, and generated more than $300 millions in total economic loss (Ellsworth et al., 2019; Lee et al., 2019). The hypocenter was located approximately 10 km northeast of Pohang city, close to the Pohang Enhanced Geothermal System (EGS) site (36.106°N, 129.373°E and depth ~4.27 km, Korean Government Commission, 2019). Its proximity to the EGS site and hypocentral depth similar to the open hole sections of the fluid-injection wells (Figure 1) quickly raised questions if this earthquake is associated with EGS activities (Grigoli et al., 2018; Kim et al., 2018).

The Pohang EGS project was designed to create an enhanced geothermal reservoir within a low permeability crystalline basement. The basement is overlain by cretaceous volcanic and sedimentary rocks, tertiary volcanic and sedimentary rocks, and quaternary sediments (Ellsworth et al., 2019). During a period of four years (2012 to 2016), two geothermal wells, PX-1 and PX-2 (maximum depth ~4.3 km) were drilled for hydraulic stimulations. At the surface, both wells are separated by only 6 m distance, increasing to a separation of 599 m at a depth of ~4300 m. For well PX-1, the drilling was stuck at a depth of 2419 m, and hence side-tracked into west-northwest direction. Well PX-2 experienced large mud loss in the depth interval 3830 - 3840 m, while cuttings contain significant fractions of friable round-shaped mud balls typical for fault gouge (Korean Government Commission, 2019; Ellsworth et al., 2019). In these geothermal wells, five

hydraulic stimulations were conducted between 29 January 2016 and 18 September 2018. During this period, each hydraulic stimulation phase was associated with seismicity. The magnitudes during and after stimulations reached up to $M_L \approx 3$, while events were distributed within a restricted area close to the wells (Woo et al., 2019). The depth of the seismicity before the Pohang earthquake spans the depth range 3.8 to 4.4 km, comparable with the open-hole section of the well at ~4.3 km depth (Ellsworth et al., 2019).

Recent studies confirm that the Pohang earthquake was induced by hydraulic stimulation and extensive fluid injection at this EGS site (Korean Government Commission, 2019; Ellsworth et al., 2019; Woo et al., 2019; Kim et al., 2020). These activities are considered to have activated the previously unmapped fault which was found to intersect well PX-2 at a depth of ~3.8 km. Chang et al. (2020) point out that increased pore-pressure stressing due to multiple injection wells at the Pohang EGS site may have contributed to the mainshock generation. However, it has been argued that the size of fluid-injection induced earthquakes can be managed by controlling pressure, rate, and location of fluid injection (Hofmann et al., 2019). Data-driven empirical and numerical studies have shown that the largest induced earthquakes are bounded by a function of injected volume (McGarr, 2014; Galis et al., 2017).

Grigoli et al. (2018) find a complex-source mechanism for the Pohang earthquake with a significant non-double couple (non-DC) component. They hypothesized that this earthquake involved failure on two different faults with slightly different focal mechanisms. In fact, in EGS reservoirs with extensive fluid injection and hydraulic stimulation, earthquakes with pronounced non-DC components may occur (Julian et al., 1998). Moreover, fluid injections may induce local deviation of the stress state from the regional stress regime (Schoenball et al., 2014; Martínez-Garzón et al., 2013; Martínez-Garzón et al., 2014). Therefore, we examine how regional and local

stress conditions acting on different fault models (single plane and two planes) determine the dynamic rupture process that leads to a source mechanism with non-DC components.

Dynamic rupture modeling aims to reproduce the physical processes that govern how earthquakes start, propagate, and stop for given stress and frictional conditions acting on fault surfaces. The earthquake dynamics are then a result of the model's initial conditions, such as geometry and frictional strength of the fault(s), the tectonic stress state, the regional lithological structure, and a frictional constitutive equation. Jin and Zoback (2018) model coseismic fully dynamic spontaneous fault rupture resulting from preseismic quasi-static loading exerted by fluid perturbations in a faulted porous medium in 2D. Duan (2016) model 2D dynamic rupture accounting for fluid effects of a propagating hydraulic fracture. Cappa and Ruitquist (2012) and Buijze et al. (2017) constrain the onset of 2D dynamic rupture experiments by the stress state resulting from solving a coupled quasi-static poroelastic equation. Further 2D studies that model induced (not fully dynamic) earthquake rupture linked to separately treated fluid diffusion including Galis et al. (2017); Kroll et al., (2017); Dieterich et al. (2015); Garagash and Germanovich (2012); Richards-Dinger and Dieterich (2012); Viesca and Rice (2012). Using modern numerical methods and advanced hardware, a high degree of realism can be reached to explicitly model in 3D the highly non-linear dynamic rupture process (e.g., Heinecke et al., 2014; Roten et al., 2014; Uphoff et al., 2017; Wollherr et al., 2019; Ulrich et al., 2019a, 2019b). The modeling results include spatial and temporal evolution of earthquake rupture, surface displacements, and ground shaking caused by the radiated seismic waves.

In this study, we investigate the dynamic rupture process under variable stress and fault-geometry assumptions for the Pohang earthquake, using the high-performance-computing (HPC) enabled software package SeisSol (https://github.com/SeisSol/SeisSol). Two alternative fault

106 geometries are considered, a one fault plane model (Model 1F) and a two fault planes model
107 (Model 2F). In our simulations, we consider a 1D velocity structure (Woo et al., 2019), off-fault
108 plasticity (Wollherr et al., 2018), depth-dependent bulk cohesion, a rapid velocity weakening
109 friction law, borehole estimates of stress, complex fault geometry, and high-resolution topography.
110 In the following, we first describe (Section 2) a new observationally guided fault
111 reconstruction approach based on spatio-temporal clusters of microearthquakes and their spatial
112 uncertainty. In Section 3, we analyse initial fault strength and loading stresses using static and
113 dynamic rupture modeling. We then compare the dynamics and kinematics of two preferred
114 models, Model 1F and 2F. The validation of Model 2F with regional waveforms, as well as
115 comparison of surface deformation between Model 1F and Model 2F are also presented in Section
116 3. Finally, we discuss the importance of considering local stresses loading, apparently weak and
117 critically stressed faults, overpressurized fluids, and dynamic multiple fault interaction in EGS.
118

119 # Modeling Setup

120 In the following, we describe our approach to produce a physically viable model
121 constrained by observational data. Dynamic rupture propagation is governed by fault strength,
122 fault geometry, subsurface material properties, topography, loading ("initial") stresses, nucleation
123 procedure, and empirical friction laws (Dunham et al., 2011a; Harris et al., 2011; Harris et al.,
124 2018). Numerical experiments that vary the aforementioned parameters provide insights into
125 fundamental earthquake physics as well as serve to identify preferred, self-consistent scenarios
126 that explain the mechanical processes of the earthquake as well as observational data.
127

128 ## Fault reconstruction

The detailed fault geometry has a strong effect on the dynamic rupture process. Changes in strike, dip, and deviations from fault planarity can impact the rupture propagation and the corresponding physical processes. The Pohang earthquake occurred on one or several blind and unmapped fault(s). Because the unwrapped InSAR surface-displacement data show unclear fringes due to the small deformation around the epicenter (Choi et al., 2019; Song and Lee, 2019), we use the high-resolution earthquake catalog from Kim et al. (2018) to constrain the fault geometry based on a space-time (including their uncertainties in space) clustering approach. The earthquake catalog spans from 9 hours before to 3 hours after the mainshock and contains 217 events.

**Spatio-temporal clustering**

Clustering techniques allow deciphering complex fault structures by associating seismic events to groups (clusters), also discriminating events that are associated with the mainshock from uncorrelated earthquakes. We examine the seismic sequence to separate seismic clusters and background events using nearest-neighbor distances following Zaliapin and Ben-Zion (2013). The dependence of an event *i* to a parent event *j* is determined from the nearest-neighbor distance $\eta_{ij}$:

$$\eta_{ij} = dt_{ij} \times dr_{ij}^{d}, \; d_{ij} > 0; \quad \eta_{ij}=\infty, \quad dt_{ij} < 0 \qquad (1)$$

where $dt_{ij} = t_j - t_i$ is the time between event *i* and *j*, $dr_{ij} = (r_j - r_i)$ is the interevent distance between events; $r_i$ = coordinate of event *i* and $r_j$ = coordinate of event *j*, and *d* is the fractal dimension of the earthquake hypocenter distribution (Hirata, 1989). We find that the inferred clusters are not very sensitive to the parameter d; hence we set d = 1.6 following previous studies (Zaliapin and Ben-Zion, 2013; Zhang and Shearer, 2016; Cheng and Chen, 2018). Based on this analysis, we

find that all earthquakes of the catalog are part of the cluster and can be used for fault-plane fitting (see Figure 2a). This cluster is characterized by interevent distances less than 1 km.

**Fault plane fitting**

We adopt the anisotropic clustering location uncertainty distribution (ACLUD) method, a fault-network reconstruction approach introduced by Wang et al. (2013), which accounts for uncertainties in earthquake locations. This method is extended by considering regional tectonic constraints, focal mechanisms, and surface geological manifestation as prior information, leading to the following improvements in the original ACLUD algorithm:

1) Initialize $N_0$ number of faults following the predefined orientation of the $S_{Hmax}$ extracted from the world stress map with random position and size.
2) For each cluster, if more than four similar focal mechanisms (strike, dip, rake) are available, we use this information to separate events that have distinct focal mechanisms into other clusters.
3) If surface geological manifestation (fault traces) exists (not the case for this study), the strike and dip of the generated fault segment(s) should follow the closest interpreted fault trace orientation.

We refer to this modified ACLUD method as guided-ACLUD (g-ACLUD).

All explored solutions are subject to a statistical validation process that examines the likelihood of each proposed fault-network, given all available focal mechanisms. Statistical validation uses the Bayesian Information Criterion (BIC). Initially, the method uses a random number of fault planes. A single fault plane may be split if the BIC remains high. On the other hand, two close-enough fault planes with similar orientation (strike and dip) may be merged into

a single fault plane. The process is repeated until the BIC reaches a pre-defined minimum or if the process exceeds the maximum specified number of iterations (Wang et al., 2013).

The ACLUD algorithm by Wang et al. (2013) uses event locations and the associated uncertainties given by the earthquake catalog. We incorporate additional information to increase the robustness of the results and to decrease the explored parameter space. As *a priori* information, we use the orientation of the maximum compressive regional stress given by the world stress map (Heidbach et al. 2018) and available focal mechanisms in the area which are associated with the earthquake catalog. Therefore, we use a maximum horizontal stress orientation of 74° with an uncertainty of 25° and consider the focal mechanism inferred by Grigoli et al. (2018). Since location errors are not specified in this earthquake catalog, we assume normally distributed uncertainty for all events (standard deviation of 100 m). Note that Kim et al. (2018) obtained a median error of 42, 31, and 36 m in the EW, NS, and vertical directions, respectively, but no uncertainties for individual events.

Figure 2b, 2c, 2d show the g-ACLUD selected solution, characterized by the smallest BIC, which features two intersecting planar fault planes. The main plane strikes at 214° and dips at 65°, while the secondary fault plane strikes at 199° and dips 60°, respectively. The two fault planes are separated by a narrow angle of 15°. The secondary fault aligns with the subsidiary fault plane identified by Kim et al. (2018). The dimensions of the main and secondary fault planes are 4.3 x 2.8 km and 3.0 x 2.2 km, respectively. As the goal of this study is to compare the rupture process for two different fault configurations, we define a one fault plane geometry (Model 1F) and a two fault planes geometry (Model 2F; derived fault reconstruction analysis). The single-fault model has a fault plane striking 214° and dipping 43°, as suggested by Korean Government Commission (2019), Ellsworth et al. (2019), and Woo et al. (2019).

198

199 ## Material properties

200 We assume an elasto-plastic, isotropic medium based on the 1D velocity profile (Figure
201 S1a; Woo et al. (2019)). The velocity profile honors geological structures observed from drilling
202 cores and seismological observations from both active and passive sources, for instance, vertical
203 seismic profiling (VSP) and well logging (Korean Government Commission, 2019; Woo et al.,
204 2019). The density distribution (Figure S1a) is adopted from the report by Korean Government
205 Commission (2019).

206 We use a computationally efficient implementation of a Drucker-Prager off-fault
207 viscoplastic rheology (Wollherr et al., 2018). The off-fault failure criterion is based on the internal
208 friction coefficient (bulk friction) and bulk cohesion. We assume a constant internal friction
209 coefficient equal to the prescribed on-fault friction coefficient ($\mu_{bulk-friction} = 0.6$) for the entire
210 model domain. However, bulk cohesion is set to be depth-dependent, accounting for geologic
211 strata in the Pohang EGS site and the hardening of rocks with depth. Therefore, bulk cohesion
212 ranges from $c = 4$ MPa near the surface to $c = 50$ MPa at a depth of 6 km. A lower bulk cohesion
213 (12.5% of the surroundings) is applied in a 1.5 x 0.3 x 4 $km^3$ volume around the fault intersection
214 for the case of two fault planes to mimic pre-existing damage which enhances off-fault yielding
215 and to prevent unrealistic high on-fault stresses at the fault intersection. We assume initially
216 equivalent stresses acting on and off the fault. Finally, we set a constant, mesh-independent
217 relaxation time following the analysis by Wollherr et al., (2018) and chose $T_V$= 0.05 s, consistently
218 with choices made in previous studies (e.g. Ulrich et al., 2019a, 2019b).

219

220 ## Fault strength and loading stresses

To constrain the most viable principal stress component azimuth and the overall stress regime, we extract information (e.g., $S_{Hmax}$ orientation and fault strength) from laboratory and field observation to then perform numerical experiments. We adopt a friction law with rapid velocity weakening (adapted from Dunham et al., 2011a; see Appendix A1) which reproduces the rapid friction decrease observed in laboratory experiments at co-seismic slip rates (Di Toro et al., 2011).

We parametrize fault friction aiming for realistic levels of static and dynamic frictional resistance and stress drop. All frictional properties are detailed in Appendix A1. We apply velocity weakening ($b - a = 0.004$) across the fault (see Figure S1b) and velocity strengthening ($b - a = -0.004$) to the uppermost part of the fault, which allows for a smoother termination of the rupture there. The state evolution distance ($L$), initial slip rate ($V_{ini}$), reference slip velocity ($V_0$), steady-state friction coefficient ($f_0$), and weakened friction coefficient ($f_w$) are constant and depth-independent.

We follow the systematic approach of Ulrich et al. (2019a) to examine initial fault stress and relative apparent fault strength combining data from observations, (e.g., seismo-tectonic observations and fault fluid pressurization) and the Mohr-Coulomb theory of failure. This workflow reduces the non-uniqueness in dynamic rupture modeling parameterization by assessing that the stress state is compatible with the fault geometry and the fault-slip orientation (rake angle) inferred from finite source or moment tensor inversion. Assuming an Andersonian stress regime (one principal stress axis is vertical), only four parameters are sufficient to fully describe the stress state and strength of the fault system: the azimuth of maximum compressive stress ($S_{Hmax}$), the initial relative fault prestress ratio ($R_0$), the stress shape ratio ($\nu$), and the fluid pressure ratio ($\gamma$), all detailed hereafter.

The Pohang EGS site is considered to be located within a strike-slip stress regime (Soh et al., 2018, and references therein). This translates into the maximum principal stress being horizontal ($s_1 = S_{Hmax}$, with principal stress components $s_1 > s_2 > s_3 > 0$) under Andersonian stress. Previous studies examined the azimuth of maximum horizontal stress using different methods, such as borehole and seismological techniques, e.g., stress inversion of focal mechanisms (Kim et al., 2017; Lee et al., 2017; Lee, Hong, and Chang, 2017; Soh et al., 2018; Korean Government Commission, 2019; Ellsworth et al., 2019). Soh et al. (2018) inferred $S_{Hmax}$ from focal mechanisms of earthquakes that occurred between 1997 and 2016 and determined a regional $S_{Hmax} = 74°$. However, the earthquakes closest (~40 km) to the Pohang EGS site used in their analysis are the 2016 Gyeongju event and its aftershocks. Based on borehole data, Kim et al. (2017) and Lee, Shinn, et al. (2017) determined that $S_{Hmax}$ at shallow depths (700 m to 1000 m) within a 10 km radius from the Pohang EGS is about 130°. In contrast, Ellsworth et al. (2019) and Korean Government Commission (2019) inferred a critically stressed thrust faulting regime. This stress state implies that the vertical stress is the least principal stress under Andersonian stress ($s_v = s_3$). They inferred an $S_{Hmax}$ orientation of $77 \pm 23°$ based on dipole sonic logging data. This orientation is similar to the value of 74° given in the world stress map (Heidbach et al., 2018).

Using numerical simulations, we then assess how these loading-stress regimes for the inferred fault geometry determine nucleation and rupture of the Pohang earthquake. The stress shape ratio $\nu$ enables a contrast of different stress styles by balancing the principal stress amplitudes. It is defined as:

$$\nu = \frac{(s_2 - s_3)}{(s_1 - s_3)} \qquad (2)$$

For strike-slip regimes ($s_2$ vertical), $\nu < 0.5$ characterizes transpression, $\nu \approx 0.5$ corresponds to pure strike-slip regime, and $\nu > 0.5$ characterizes transtension (Ulrich et al., 2019a). Soh et al. (2018) ($\nu = 0.12$), Ellsworth et al., (2019) and Korean Government Commission (2019) ($\nu = 0.1$) suggests a stress regime acknowledging transpression around the Pohang EGS site (note that they use different definition of $\nu$).

The initial relative prestress ratio ($R_0$) describes the closeness to failure on a virtual, optimally oriented fault. $R_0 = 1$ indicates a critical stress level on all optimally oriented faults. We can characterize fault strength spatially by calculating the relative prestress ratio ($R$) on every point of the fault. $R$ denotes the ratio of potential stress drop $\Delta\tau$ with respect to breakdown strength drop $\Delta\tau_b$ for given frictional cohesion ($c$), static ($\mu_s$) and dynamic ($\mu_d$) friction coefficient (e.g., Aochi and Madariaga, 2003) expressed as:

$$R = \frac{\Delta\tau}{\Delta\tau_b} = \frac{\tau_0 - \mu_d\sigma_n}{c + (\mu_s - \mu_d)\times\sigma_n} \quad (3)$$

where $\tau_0$ and $\sigma_n$ are initial shear and normal traction on the fault plane, respectively. However, in this study, we neglect the contribution of frictional cohesion ($c = 0$), which is mostly important to incorporate close to the Earth's surface. We assume $\mu_s = f_0 = 0.6$ and $\mu_d = f_w = 0.1$. The relative prestress ratio can be related to the relative fault strength parameter ($S$) defined as $S = 1/R - 1$. On-fault values of $R$ change at every point as we vary $R_0$, taking on values $R \leq R_0$ depending on the orientation of each fault point with respect to the optimal orientation.

The vertical principal stress is assumed to vary linearly with depth, consistent with the geological strata (depth-dependent density ($\rho$) in Figure S1a). We assume the intermediate principal stress component, $s_2$, to be vertical. The confining pressure of the overlying rock is

reduced by the pore pressure ($P_f$). We assume $P_f$ proportional to lithostatic stress as $P_f = \gamma\rho g z$, where $g$ is the gravitational acceleration (9.8 $m/s^2$), and $z$ denotes depth (in meters) and $\gamma$ is the fluid pressure ratio. A fluid pressure ratio of 0.37 indicates hydrostatic pore pressure, while $\gamma >$ 0.37 implies an overpressurized stress state.

We perform a range of static and dynamic numerical experiments described below to test the sensitivity of the resulting dynamic rupture models to the chosen stress parameterization in terms of $S_{Hmax}$, $R_0$ and $\gamma$. We keep the 4th parameter, the stress shape ratio, fixed at $\nu = 0.12$ (Soh et al., 2018). We do not adjust the stress states for the stress excess during nucleation (see Appendix A2). The overstressed nucleation and its parameters are constant for all 180 numerical experiments.

# Results

We use the open-source software SeisSol (details in Appendix A3, **numerical method**) to solve the elastodynamic equations of motion for fault rupture under stress and friction acting on the fault surface, coupled to seismic wave propagation in complex media. We set the on-fault mesh size using estimates of cohesive zone width (details in Appendix A3, **mesh generation**). We incorporate high-resolution topography into our modeling. Figure 3 shows the computational mesh overlain by a snapshot of absolute velocity at t = 5 s.

Next, we present 3D dynamic rupture simulations for scenarios that consider one and two intersecting fault planes, incorporating depth-dependent regional loading stresses, off-fault plastic yielding, and high-resolution surface topography. In the preferred model (Model 2F), the secondary fault plane is dynamically triggered and can explain the observed non-double couple

312 component of the moment tensor solution. Our model is compatible with regional waveforms and
313 surface deformation derived from published InSAR analysis.
314

315 ## Static and dynamic analysis of initial fault strength and stresses

316 We first constrain the regional stress from purely static analysis. Figure S2 shows a few
317 cases (out of many permutations (see also Table S1)) we analyzed. The six examples shown use
318 parameters $\gamma = 0.5$ and $R_0 = 0.7$, and variable $S_{Hmax}$ in the range 52° - 140°. According to the
319 static analysis, $S_{Hmax} < 87°$ is insufficient to generate a rake angle of shear traction compatible
320 with the thrust-faulting component inferred by the focal mechanism and moment tensor solution.
321 At $S_{Hmax} \geq 87°$, a thrust-faulting component starts to emerge. Interestingly, only the secondary
322 fault plane features a rake angle larger than 40° for $S_{Hmax} = 77° - 140°$. A rake angle of ~ 80°,
323 obtained with $S_{Hmax} = 120°$, can potentially produce the thrust-faulting component inferred by
324 moment tensor solution. For this parametrization, the secondary fault plane reaches a higher rake
325 angle of approximately 110°.

326 We restrict the parameter space for $R_0$ and $\gamma$ based on our static analysis. We then
327 systematically explore all permutations of the three different parameters within the selected range
328 using dynamic rupture simulations. We vary $R_0$ in the range 0.7 - 0.9, $\gamma$ within 0.37 - 0.9 and
329 $S_{Hmax}$ within 67 - 120°. Figure 4 summarizes the outcome of 180 numerical dynamic rupture
330 experiments. We find that under hydrostatic pressure ($\gamma = 0.37$), $S_{Hmax} = 120°$ generates self-
331 sustained ruptures over any other $S_{Hmax}$ orientation.

332 The thrust-faulting component generated with $S_{Hmax} = 67° - 87°$ is insufficient to
333 explain the seismological observation using dynamic rupture modeling. Such $S_{Hmax}$ leads to pure
334 strike-slip faulting as the only mechanical viable solution. Both dynamic and static analyses

suggest that $S_{Hmax} = 120°$ is necessary to generate a thrust-faulting component close to the observations. Our analyses allow determining a preferred parameterization, compatible with inferred ground deformation, observed regional waveforms, and the inferred focal mechanism: $R_0 = 0.8$ and $\gamma = 0.5$.

## Rupture dynamics of the preferred scenario Model 1F and Model 2F

Figure 5a and movie M1 (in supplementary material) provide an overview of the simulated earthquake rupture of the preferred two fault model Model 2F: rupture propagates spontaneously across the main fault plane and dynamically triggers the secondary fault plane (rupture jumping).

The rupture nucleates smoothly due to the prescribed time-dependent overstress (see Appendix A2) centered at the hypocenter location; it then spontaneously propagates bilaterally across the main fault plane. At a rupture time of 0.65 s, two successive slip-rate fronts emerge, with lower peak slip rates than the main rupture front (Figure 5a, left). This rupture complexity is associated with the simultaneous rupture on both fault planes, leading to multiple reflected and trapped waves in-between the two fault planes, reactivating the main fault around the intersection. Rupture complexity decreases as rupture on the secondary fault plane terminates. After rupture time t = 0.75 s, we observe solely pulse-like rupture propagation across the main fault.

The secondary fault plane is dynamically triggered at 0.4 s and its rupture terminates at 0.8 s simulation time, while the main-fault is fully ruptured in about 1.1 s. The secondary fault plane is only partially ruptured because the northern part of the main fault does not slip. High slip-rates (~ 10 m/s) and multiple rupture fronts occur near the fault intersection at the secondary fault. Rupture heals close to the fault intersection region around $t = 0.65\ s$.

After $t = 0.75\ s$ rupture on the main fault dynamically clamps (e.g., Kyriakopoulos et al., 2019) and thus does not facilitate direct branching to the northern unbroken part of the secondary fault plane. We observe asymmetric peak slip-rate distribution (see Figure S3), with higher values on the single fault plane part of the network (Figures 5a, right) and lower peak slip rates where ruptures across directly adjacent fault planes interact, which is also associated with high off-fault plastic yielding (see section **Off-fault deformation** below). The entire rupture is completed after ~1.5 s simulation time, breaking 4 km of fault length and generating a moment magnitude of $M_w$ 5.59 (dominated by slip on the main fault plane). We find that rupture stops smoothly and spontaneously on the secondary fault plane and north-eastern part of the main fault plane, while being stopped abruptly by the southwestern fault end of the main fault plane.

In contrast to the Model 2F, the one fault plane preferred Model 1F produces symmetric bilateral slip-rate and slip distributions.

## Rupture kinematics of the preferred Model 1F and Model 2F scenarios

Due to the size of the event and limited available data, the kinematics of the Pohang earthquake are challenging to characterize and explain. We here describe the model kinematics of the preferred Model 1F and Model 2F earthquake scenarios. and compare both with two observational studies (Song and Lee, 2019; Grigoli et al., 2018).

Song and Lee (2019) estimated the static slip distribution by InSAR (both descending and ascending-descending orbit) for a single fault plane with patch size 0.5 km by 0.5 km. Higher slip predominantly occurs northeast of the hypocenter, with an average slip of 0.15 m (Song and Lee, 2019). Grigoli et al. (2018) applied an Empirical Green's Function (EGF) technique to study rupture duration and directivity, suggesting an apparent rupture duration of ~1s and ~3 s for

stations observed in the SE and NW direction, respectively. Their focal mechanism shows an average rake of ~135°.

Both preferred scenarios vary slightly in moment magnitude, $M_W$ 5.63 and $M_W$5.59 for Model 1F and Model 2F, reflecting different fault geometries while otherwise using the same dynamic rupture model parametrization. We point out that most slip of Model 2F occurs on the main fault - its magnitude is reduced to $M_W$5.51when removing the subsidiary plane.

The resulting synthetic source time functions of Model 1F and Model 2F are presented in Figure 7a and 7b, respectively. The boxcar shaped moment rate function of Model 1F results from its comparably simple rupture dynamics across one planar fault. Model 2F features a more complicated moment rate function featuring two peaks of which the first one is reached at t = 0.5 s simulation time during simultaneous rupture of both fault planes. The rupture duration of both scenarios is less than 1.5 s. The moment tensor representations of Model 1F and Model 2F are presented in Figure 7c and 7d, respectively. Both scenarios show oblique faulting mechanisms. Model 1F clearly produces a double-couple moment tensor solution (Figure 7c), whereas the Model 2F yields a non-double couple solution due to complex source mechanism (Figure 7d), in agreement with Grigoli et al. (2018). Nevertheless, our simulation produces a smaller amount of CLVD (compensated linear vector dipole) compared to Grigoli et al. (2018). In fact, the equivalent moment tensor solution of Model 2F can be decomposed, following the methodology of Vavryčuk (2015), into 82.95% DC, -5.05% CLVD, and -12% isotropic (ISO) components. In contrast, Grigoli et al. (2018) find -37% CLVD. In our simulations, Model 2F's rupture is characterized by an average rupture speed of $v_r \approx 2{,}250\ m/s$, well below the average Rayleigh wave speed at the depth of the faults ($v_r \sim 0.75V_S$). The spatial variation of $v_r$ is mainly related to the complexity of rupture around the intersection for both, the main and secondary fault plane. We observe higher

403 average rupture speed $v_r \approx 2{,}780\ m/s$ ($v_r \sim 0.8V_S$) on the secondary fault plane (see rupture
404 contours every 0.2 s in Figures 5a, 5b). We note the localized occurence of supershear rupture
405 speeds ( $\sim 4000\ m/s$) near the edge of the prescribed nucleation patch of the main fault reflecting
406 the high overstress required for initiating the preferred rupture dynamics in our setup. Also, the
407 secondary fault plane features localized supershear episodes ($\sim 3800\ m/s$). In our model setup,
408 this may be translated into locally high fluid overpressure, and/or reflect the low resolution and
409 1D restriction of the used velocity model. More complex fluid effects have been shown to
410 transition sub-rayleigh to supershear ruptures in fully coupled 2D models by Lin and Zoback
411 (2018).

412 In our preferred model, high slip ($\sim 2\ m$) occurs in the center of the main fault. We observe
413 a maximum slip of 1.3 m at the secondary fault plane (Figure 6b). In total, the average on-fault
414 slip is 0.32m. Both, Model 1F and Model 2F, feature higher slip than Song and Lee (2019) infer
415 in their static slip inversion. In addition, differences may arise due to different modeling
416 assumptions in terms of fault dimensions and shear moduli. First, Song and Lee (2019) assume a
417 slightly larger shear modulus of G = 30 GPa than in our model (G = 26 GPa). Second, they assume
418 a single fault plane of significantly larger dimensions (6 x 5 km) than the faults of our models (see
419 section **Fault reconstruction**). This large fault geometry allows for the possibility of near-surface
420 slip.

421 The orientation of fault slip is modulated by the dynamic source process. The dynamic
422 interaction of the two fault planes induces a moderate thrust-faulting component (rake $\sim 135° - 150°$) on the main fault plane, as well as complex time-dependent rake orientations on the
424 secondary fault (see also Figure 6c, 6d). In contrast to Model 2F, the orientations of the final rake
425 angle of Model 1F are distributed homogeneously, on average at 127°. The rake of Model 1F is

426 different from Model 2F due to different dip angles of the main fault which dips at 43° in Model
427 1F. This average rake angle is comparable to the focal mechanism derived by Grigoli et al. (2018).
428 The average on-fault slip is 0.35 m. We observe that, on average, the rupture speed is $v_r \approx$
429 2400m/s. Reflecting similar dynamic parameters to Model 2F, Model 1F also experiences
430 supershear rupture near the nucleation patch.
431

## 432 Waveform comparison for Model 1F and Model 2F

433 In the following, we analyze the differences between Model 1F and Model 2F in terms of
434 near and far-field ground motion. Hereinafter, all distances from the fault are considered as Joyner-
435 Boore distances ($R_{JB}$, the shortest distance from a site to the surface projection of fault planes).
436 We compare synthetic waveforms computed for hypothetical ("virtual") stations located close (~4
437 km) and far (>20 km) from the epicenter.
438 Figure 8b shows three-component waveforms at 19 randomly located virtual stations
439 (Figure 8a). We place 10 stations near the epicenter (~4 km horizontal distance) to inspect near
440 field seismic waveform characteristics. We filter all synthetic waveforms within the frequency
441 band of 0.1 - 2 Hz using a fourth-order Butterworth filter. Figure 8c depicts all 3-component
442 velocity waveforms. Overall, waveforms of scenarios Model 1F and Model 2F are very similar in
443 this frequency range, but waveforms from Model 1F have systematically higher amplitudes than
444 Model 2F. The most remarkable amplitude differences occur on the EW component for stations
445 004, 008, 009, and 010, which are all located above or close to the faults.
446 At some stations, distinct waveform differences appear (e.g., the NS-component of stations
447 007, 014, 011, and 019). Most of these stations are located on the hanging wall. After five seconds,
448 once the rupture is fully arrested, differences vanish, and the waveforms become comparable for

449 both models. As depicted in Figure 8b, the stations located close to the region where faults overlap
450 in Model 2F show significant differences in seismic wave signatures on the horizontal components.
451 One possible explanation may be that the additional secondary fault defocuses ground motions.
452

453 ## Off-fault deformation

454 Our preferred dynamic earthquake rupture model 2F reveals significant off-fault plastic
455 deformation in the vicinity of geometric fault complexity, similar to scenarios of the 1992 Landers
456 earthquake (Wollherr et al., 2018), the 2016 Kaikoura earthquake (Klinger et al., 2019) and the
457 2019 Ridgecrest earthquake sequence (Taufiqurrahman et al., 2019). Here, significant off-fault
458 plastic deformation (quantified as the scalar quantity $\eta$ following Ma, 2008 and Wollherr et al.,
459 2019) occurs (i) in the pre-existing damage zone at the fault intersection, (ii) at the dilatational side
460 of the main and the secondary fault as expected from previous theoretical and numerical studies,
461 given the shallow angle of both faults and $S_{Hmax}$ (Templeton and Rice, 2008; Gabriel et al., 2013),
462 and (iii) close to the free-surface (see Figures S3c and S3d).

463 The fault intersection of Model 2F elevates the total off-fault plasticity response
464 regularizing high on-fault stresses while limiting peak slip rates and reducing peak ground motions
465 (Andrews 2005; Dunham et al. 2011a; Gabriel et al., 2013; Roten et al., 2014; Wollherr et al.,
466 2018). When comparing waveforms, we indeed notice overall lower velocity amplitudes compared
467 to Model 1F in the surrounding stations of the fault planes caused by the combined effects of fault
468 complexity and off-fault yielding. Interestingly, the stronger plastic yielding response in model 2F
469 leads to lower variability (not shown here) in ground motions (PGV) (as in Wollherr et al., 2019)
470 even though the fault geometry is more complex.
471

## Model 1F and Model 2F surface deformations

Next, we compare the co-seismic surface displacement generated by Model 1F to Model 2F (Figure 9a, 9b). We translate the synthetic vertical and horizontal displacements into Line-of-sight (LoS) displacement components.

The spatial distribution of the co-seismic surface deformations is noticeably different. Model 1F features higher LoS displacements in southeastern direction relative to the Gokgang Fault ($\sim 2\ km$ from the bay) compared to Model 2F ($\sim 5\ km$ from the bay) and generates on average lower negative LoS displacements. Model 1F creates a wider area of uplifted LoS displacements, which resembles an ellipse with a major axis of 6 km and a minor axis of 4.1 km. The most prominent spatial differences are (i) the vertical LoS displacements of Model 1F are slightly migrated to the East relative to the epicenter and (ii) the location of zero displacements in between vertical LoS displacements (in the region of the epicenter) and negative LoS displacements at the eastern-to-southward of the epicenter. Model 2F produces an average of 5 cm subsidence whereas Model 1F only produces 2 cm average subsidence. This can be attributed to Model 1F's more shallow dipping angle. The co-seismic surface displacements of Model 2F compare better than those of Model 1F to InSAR ground deformation inferences of Song and Lee (2019), in terms of the location of the pivot line delimiting positive and negative LoS displacements ($\sim 4.5\ km$ from the bay).

While synthetic (Model 2F) and observed surface displacements significantly differ locally and quantitatively, they reveal qualitatively comparable large-scale features. The following observations are captured by Model 2F: (i) Uplift/easting displacement is observed near the epicenter and (ii) the uplifted area forms an ellipse-like shape with a major axis of ~5.6 km and a minor axis of ~3.8 km. Correspondingly, Pohang city also experienced subsidence according to

field observations (Kang et al., 2019a, Kang et al., 2019b). Additionally, our synthetics also suggest subsidence underneath the bay.

Although the contribution of the secondary fault plane is critical to reproduce the inferred non-DC component, comparison of synthetic co-seismic surface displacements of Model 2F with and without the secondary fault (see Figure S5a) suggests that the contribution of the secondary fault plane to the ground displacement is small (Figure S5b), as expected from its small slip contribution. We note that the InSAR data may not be sensitive enough to discriminate between a one and a two-fault plane model.

## Model 2F validation by regional waveform modeling

Unfortunately, a local seismic network of eight portable seismic stations (Kim et al., 2018) deployed around the EGS site produced saturated (clipped) seismograms. Therefore, we choose to compare synthetic waveforms to regional recordings at five stations surrounding the Pohang EGS site (see Figure 1) at epicentral distances of approximately 70 km.

Model 2F compares well to regional low-frequency seismic wave observations (Figure 8c). Synthetic waveforms are calculated using a Green's function database of teleseismic waveforms (Instaseis, Krischer et al., 2017). We translate the dynamic rupture model into a single moment tensor representation following Ulrich et al. (2019a, 2019b). The Green's function database we use is based on the anisotropic Preliminary Reference Earth Model (PREM), and is accurate to a maximum period of 2 s. Synthetic and observed waveforms are filtered using a 0.033 - 0.08 Hz $4^{th}$order Butterworth filter, equivalent to the frequency band used in the source inversion of Grigoli et al. (2018). The goodness of fit is assessed by the root-mean-square (rms) misfit.

Although the synthetic waveforms compare reasonably well to regional recordings, we find that a few synthetic amplitudes are systematically larger than the observed data. We attribute this to the usage of a 1D PREM model, which is more suitable for modeling synthetics at larger azimuthal distance. Additionally, the fact that our simulation returns a slightly higher seismic moment than observed and is not able to capture the full non-DC component of the source may play a role. In particular, the large misfit at Station TJN on the UD and EW component may be attributed to unmodeled site effects. Our synthetics do not differ significantly from the synthetics of Grigoli et al. (2018), derived by full-waveform inversion of the waveforms recorded at stations BUS2, CHJ2, and NAWB. A significant difference is only noticeable on the NS component of station BUS2 (south of the epicenter, Figure 1).

# Discussion

## The importance of local stresses for rupture dynamics in EGS

The inferences of previous studies vary in terms of stress regimes and maximum horizontal stress orientation around the Pohang EGS site, thereby motivating our systematic numerical experiments as detailed in section **Static and dynamic analysis of initial fault strength and stresses** under various loading stress settings. Assuming an Andersonian stress regime, we find that an initial stress state constrained by regional stress inversions is unable to generate the observed thrust-faulting component of the Pohang earthquake. This suggests important local deviations from the regional stress state near the Pohang EGS site. Kim et al. (2017) and Lee et al. (2017) infer the stress orientation at short epicentral distance (< 10 km) from borehole image log data acquired prior to the Pohang earthquake. However, this data is limited to 1 km depth, whereas

539 the Pohang earthquake hypocentral depth is inferred to be deeper, at a depth of 4.27 km. Ellsworth
540 et al. (2019) noted that the in-situ stress state at the Pohang EGS site is transpressional.

541 From our static numerical experiments, we infer that a pure strike-slip stress regime ($s_2 =$
542 $s_v$) and $S_{Hmax} = 120°$ yield a thrust-faulting component consistent with observations (Figure S2).
543 This finding is corroborated by our dynamic rupture simulations under identical loading (Figure
544 7c, 7d). We also observe that under these conditions spontaneous rupture propagation is favoured.
545 The reverse faulting regime ($s_3 = s_v$) accounting for low $\nu = 0.1$ was also explored. However,
546 such reverse-stress regime, as suggested by Ellsworth et al. (2019), across the entire fault planes
547 does not yield sufficiently high shear tractions on our fault system - and dynamic rupture dies out
548 quickly.

549 Local variations of the stress state around EGS sites, including the Pohang EGS site, have
550 been observed in hydraulic stimulation experiments of crystalline-rock reservoirs (Schoenball et
551 a., 2010), data-driven geomechanical analysis (Ceunot et al., 2006; Hardebeck and Michael, 2006;
552 Martínez-Garzón et al., 2013; Martínez-Garzón et al. 2014; Schoenball et al., 2014) and numerical
553 experiments (Jeanne et al., 2015; Ziegler et al., 2017). Such spatial and temporal stress
554 reorientation is typically a direct response to hydraulic stimulation and fluid injections (Cornet et
555 al., 2007; Schoenball et al., 2010; Schoenball et al., 2013; Ziegler et al., 2017, Liu and Zahradnik,
556 2019). In the geothermal field surrounding the Geysers in California, Martínez-Garzón et al.
557 (2014) found that the stress regime changed from normal-faulting to strike-slip near the injection
558 wells. At the Pohang EGS site, local variations in the stress regime have been inferred from focal
559 mechanisms of microearthquakes before and after the Pohang earthquake. Woo et al. (2019)
560 reported strike-slip faulting north from the hypocenter to strike-slip associated thrust-faulting and
561 pure thrust-faulting components towards the South before the mainshock. After the mainshock

562 occurred, aftershock focal mechanisms were mainly strike-slip in the SW to oblique faulting in the
563 NE (Kim et al., 2020). Changes in the stress orientation and regime near the hypocenter prior to
564 the mainshock could correspond to hydraulic stimulation and fluid injections (Martínez-Garzón et
565 al., 2014; Liu and Zahradnik, 2019). However, the aftershock source characteristics are probably
566 related to co-seismic stress rotation.

567 Based on our analysis of various numerical experiments, we deduce that our models are
568 highly sensitive to variations in the initial stress state, and therefore allow to finely constrain the
569 fault stress loading parameters. For example, a small change in $S_{Hmax}$ may induce a significant
570 change in the modeled focal mechanism. All faults are exposed to the same local stress regime
571 while experiencing varying ratios of shear and normal loading depending on their orientation
572 towards this loading. Even a small change in fault geometry (e.g., in strike, dip, size, and the angle
573 between fault planes) strongly affects the dynamic rupture result (e.g., Yamashita and Umeda,
574 1994; Aochi et al., 2005; Bhat et al., 2007; Ulrich et al., 2019a; van Zelst et al., 2019), as here
575 illustrated when comparing Model 1F and Model 2F. We point out that trade-offs between the
576 inferred stress state and fault geometry can be readily explored if new observations become
577 available.

578 In summary, these observations support our assumption on the loading stress, which is
579 consistent with Ellsworth et al. (2019) in the nucleation region, but differently oriented everywhere
580 else. Complexities in the in-situ stress state are expected in the region where the Pohang earthquake
581 occurred, due to the history of hydraulic stimulations, that is, the EGS operation itself perturbs the
582 local stress conditions in a manner that makes it more difficult to assess the potential seismic
583 hazard implication (that are usually studied in advance and utilize regional stress information).
584

## The importance of critically stressed, static and dynamic weak faults and overpressurized fluids

Our experiments (Figure 4) emphasize the necessity of assuming overpressurized fluids ($\gamma > 0.37$) and a close to critical stress state when assuming strong frictional weakening on the fault(s). A critically stressed state has been suggested by Ellsworth et al. (2019) by analyzing dipole sonic logging data at the Pohang drilling site. In our preferred Model 2F, we use the ratio of shear over effective normal stress ($\tau/\sigma_n$) to quantify fault strength, and find 0.54 and 0.59 for the main and secondary fault plane, respectively. This fault strength is close to the assumed steady-state friction coefficient ($f_0 = 0.6$) which indicates that the faults are close to failure prior to rupture nucleation and thus close to critically stressed.

In our preferred model both faults are non-optimally oriented with respect to the local stress conditions. The relative prestress ratio $R$ is 0.35 on the main fault and 0.4 on the secondary fault plane, which is less than our assumed $R_0 = 0.8$. According to Andersonian faulting theory, the fault strength is related to its orientation with respect to the regional stress. Here, the main fault plane is oriented at 54° and the secondary fault at 60° relative to the regional maximum compressive stress ($S_{Hmax}$ = 77°). Thus, the two fault planes system would be considered weak in the classic, static sense.

All modeled faults in this study weaken dramatically at co-seismic slip rates while stress drops are limited by the elevated fluid pressure. Besides resembling the dramatic friction decrease observed in laboratory experiments and the theory of thermal weakening processes, previous dynamic rupture studies utilizing rapid velocity weakening with low values of fully weakened friction coefficient ($f_w$) reproduced rupture complexities, such as rupture reactivation and pulse-like ruptures, without assuming small-scale heterogeneities.

608 In our simulation, we use a fluid pressure ratio of 0.5 which corresponds to a reduction of
609 the normal stress of approximately 14.3 MPa compared to a hydrostatic state. The reduction in
610 effective normal stress mechanically lowers the static strength of faults. Our assumption of high
611 fluid pressure may relate to various episodes of drilling mud loss on 30-31 October 2015 at 3800
612 m depth suggesting an increase of fluid pressure on the order of 20 MPa around the borehole, and
613 the fluid injection operations (Ellsworth et al., 2019; Korean Government Commission, 2019).
614

615 **The importance of fault interaction for the dynamic rupture process and**
616 **faulting mechanism**

617 In our preferred model, the secondary fault is only partially ruptured during the Pohang
618 earthquake. Strong variations in slip rate associated with dynamic rupture complexity across the
619 two faults planes and their interaction, spontaneous rupture arrest and the asymmetrically
620 accumulated fault slip on the main and secondary fault plane, could potentially favor dynamic and
621 static Coulomb stress transfers enabling a later activation of the unruptured area of the secondary
622 fault. The largest aftershock that occurred less than three hours after the mainshock at 650 m
623 epicentral distance to the northwest with respect to the mainshock may have occurred in such an
624 unruptured area on the secondary fault.

625 In our model, complex shear faulting across two fault planes induces a non-DC component,
626 which is, nevertheless, considerably smaller (14%) compared to the CLVD component inferred by
627 Grigoli et al. (2018). Additional factors not considered in this study may contribute to an apparent
628 non-DC component, such as strong deviations from fault planarity (larger scale curvature and
629 small-scale roughness, e.g., Bydlon and Dunham, 2015; Shi and Day, 2013; Ulrich and Gabriel,
630 2017; Mai et al., 2018), stronger heterogeneities in fault stress and strength (Ripperger et al., 2008)

631 and 3D subsurface structure (e.g., Pelties et al., 2015) increasing rupture complexity, as well as
632 incorporating tensile faulting, poroelastic rheology, and source or propagation anisotropy (Julian,
633 1998; Boitz et al., 2018). The CLVD contribution may also increase when assuming a larger
634 number of faults. While the limited data available does not suggest rupture of additional fault
635 planes, stochastically distributed and dynamically activated fracture networks (e.g., Okubo et al.
636 2019; Anger and Gabriel, 2019) around the main fault are expected given the on-going stimulation
637 operation.
638

639 ## Importance of dense seismic monitoring during EGS projects

640 The complex interaction of local stress loading and fault strength conditions, rupture
641 dynamics and fault interaction on multiple fault segments presented here highlights the importance
642 of a dense local seismic network within the operational areas for monitoring and analyzing
643 microseismicity before, during, and after EGS operation, to thereby mitigate the potential seismic
644 hazard. Pre-EGS stimulation seismic monitoring is needed to define the 'unperturbed state' of the
645 system (the rock volume to be stimulated) and for characterizing potentially unmapped fault(s)
646 that may interact during cascading rupture; such seismic monitoring may be accompanied by
647 detailed borehole logging to assess the local stress state prior to stimulation.

648 During the stimulation and operational phase, a dense seismic monitoring network is also
649 needed to facilitate high-precision and high-fidelity seismic source studies. In conjunction with
650 detailed operational fluid-injection parameters, the reservoir stress state and its susceptibility for
651 generating earthquakes can be assessed (Galis et al., 2017; Kwiatek et al., 2019). In fact, the
652 available recordings of the operational monitoring seismic network near the Pohang EGS site were
653 saturated (clipped) by the unexpected high magnitude earthquake, thus accelerometers would be

654 useful as complementary instruments in EGS monitoring networks. In addition, the rise of
655 Distributed Acoustic Sensing (DAS) opens new opportunities as an additional seismic monitoring
656 network especially for EGS that is located in urban areas (Zhan, 2019).

657 Our study suggests that fully physics-based numerical simulations prior, during and after
658 an EGS project may be useful to not only gain a first-order understanding of potential effects and
659 consequences of the EGS experiments (e.g., risk-prone area as reflected by peak ground motions
660 (PGVs, Figure S6)), but also to optimally design the seismic monitoring network to ensure that all
661 vital data are collected as needed for future monitoring and mitigation purposes.

662

# 663 Conclusions

664 A guided fault reconstruction approach that clusters spatio-temporal aftershock locations
665 accounting for their uncertainty is applied to create a two fault planes dynamic rupture model
666 which reproduces key characteristics of the Pohang earthquake. Rupture complexity is arising from
667 the dynamic interaction of two failing fault planes with shallow intersection angles.

668 Static Mohr-Coulomb failure analysis and 180 numerical simulations demonstrate that the
669 regional loading stress is unable to generate dynamic rupture consistent with the observed faulting
670 style. Resolving the regional tectonic stress field onto one fault of a geometry as suggested by
671 Korean Government Commission (2019), Ellsworth et al. (2019), and Woo et al. (2019) or onto
672 the reconstructed two fault planes leads inevitable to pure strike-slip faulting, in stark contrast to
673 the observed thrust-faulting mechanism. Instead, local stress variation relative to regional stress
674 orientation is needed to generate oblique faulting. We conclude that regional-stress orientation
675 may be misleading when assessing propensity for failure; this has important implications for
676 seismic hazard assessment. Also, overpressurized pore fluids, non-optimally oriented and

dynamically weak faults and a close to critical local stress state play major roles for our dynamic rupture models of the Pohang earthquake. Such factors may be assessed when planning and conducting EGS-type experiments, explorations, and operations.

Our dynamic rupture simulations reveal dynamic triggering from the main fault plane to the secondary fault plane without direct rupture branching but via "rupture jumping". The preferred two fault plane simulation compares well to regional observed data such as moment release and far-field seismic waveforms. The single fault plane model, on the other hand, is unable to reproduce the observed non-DC focal mechanisms and surface displacement distributions due to simplicity of the dynamic rupture process and a shallower dip angle, respectively. Dynamic fault interaction, amplified by rapid stress changes due to seismic waves reverberating between the two fault planes, are needed to reproduce observations of a strong CLVD component. However, two simultaneously breaking fault planes cannot fully explain the observed source complexity.

We demonstrate the maturity and feasibility of high-resolution 3D modeling of rupture dynamics and seismic wave propagation accounting for the complexity of EGS environments and constrained by few observational parameters shedding light on the dynamics of induced and triggered earthquakes. More sophisticated 3D models, fully coupling dynamic earthquake rupture and seismic wave propagation with co-seismic and quasi-static fluid effects, such as poroelasticity, thermal pressurization, pore pressure diffusion, and considering the geometric complexity of networks of fractures and non-planar faults, may allow in future to capture the full physical complexity of nucleation and dynamics of induced earthquakes.

In the near future, such physics-based approaches may be synergistically integrated with near-field seismic monitoring before, during, and after EGS operation, thus complementing traffic light systems for hazard and risk mitigation (Bommer et al., 2006; Mignan et al., 2015).

700

# 701 Data and resources

702 All regional waveforms used in this study were downloaded from Incorporated Research
703 Institutions for Seismology (IRIS; https://www.iris.edu (last accessed February 2020)) data
704 management system using FDSN client. PREM anisotropic 2 s can be downloaded in the IRIS
705 data services products (http://ds.iris.edu/ds/products/syngine/ (last accessed February 2020)). All
706 parameters used for the preferred Model 2F are available at
707 (https://drive.google.com/open?id=1nm3HZ_YOD-j8t_YatTFfs9prVKplEExj). The
708 supplemental for this article provides additional figures, a table, and a movie mentioned in the
709 article.

710

# 711 Acknowledgments

712 We thank Xing Li and Prof. Sigurjón Jónsson for the discussions regarding surface deformations
713 using InSAR. We also thank Prof. Guy Ouillon for providing us the raw code of ACLUD. We
714 acknowledge Dr. Seok Goo Song and Prof. Hoonyol Lee for sharing the processed InSAR images
715 and discussions about inversion parameters. Computing resources were provided by King
716 Abdullah University of Science and Technology, Thuwal, Saudi Arabia (KAUST, project k1219
717 and k1343 on Shaheen II). The work presented in this paper was supported by The KAUST grants
718 (FRAGEN, ORS-2017-CRG6 3389.02), URF/1/3389-01-01, and BAS/1339-01-01. J.A.L-C has
719 also received funding from the European Union's Horizon 2020 research and innovation
720 programme under the Marie Skłodowska-Curie grant agreement Nº 754446 and UGR Research
721 and Knowledge Transfer Found – Athenea3i; and by the Deutsche Forschungsgemeinschaft (DFG,

722 German Research Foundation) – Projektnummer (407141557). TU and A.-A.G acknowledge
723 additional support by the European Union's Horizon 2020 research and innovation program
724 (ChEESE, grant no. 823844) and the European Research Council (TEAR, ERC Starting grant no.
725 852992). Part of the analysis was implemented using ObsPy (Beyreuther et al., 2010). Figures
726 were prepared using Paraview (Ahrens et al., 2005), Generic Mapping Tools (Wessel et al., 2013)
727 and Matplotlib (Hunter, 2007)

728

729 # References

730 Ahrens, J., B. Geveci, and C. Law, 2005, ParaView: An end-user tool for large-data
731 visualization, in Visualization Handbook, Elsevier Inc., 717–731.

732 Andrews, D. J., 2005, Rupture dynamics with energy loss outside the slip zone, J. Geophys. Res.,
733 110, no. B1, B01307, doi: 10.1029/2004JB003191.

734 Anger, S. and A.-A Gabriel (2019). Dynamic earthquake rupture across complex 3D
735 fracture networks. S55E-0444 presented at 2019 Fall Meeting, AGU, San Francisco, CA, 9-
736 13 Dec.

737 Aochi, H., and R. Madariaga, 2003, The 1999 Izmit, Turkey, earthquake: Nonplanar fault
738 structure, dynamic rupture process, and strong ground motion, Bull. Seismol. Soc. Am., 93,
739 no. 3, 1249–1266, doi: 10.1785/0120020167.

740 Aochi, H., O. Scotti, and C. Berge-Thierry, 2005, Dynamic transfer of rupture across differently
741 oriented segments in a complex 3-D fault system, Geophys. Res. Lett., 32, no. 21, L21304,
742 doi: 10.1029/2005GL024158.

743 Bauer, A., Scheipl, F., Küchenhoff, H., and Gabriel, A.-A. (2018). An introduction to
744 semiparametric function-on-scalar regression. Statistical Modelling, 18(3–4), 346–364.
745 https://doi.org/10.1177/1471082X17748034.

746 Beyreuther, M., R. Barsch, L. Krischer, T. Megies, Y. Behr, and J. Wassermann, 2010, ObsPy: A
747 python toolbox for seismology, Seismol. Res. Lett., 81, no. 3, 530–533, doi:
748 10.1785/gssrl.81.3.530.

749 Bhat, H. S., M. Olives, R. Dmowska, and J. R. Rice, 2007, Role of fault branches in earthquake
750 rupture dynamics, J. Geophys. Res., 112, no. B11, B11309, doi: 10.1029/2007JB005027.

751 Boitz, N., A. Reshetnikov, and S. A. Shapiro, 2018, Visualizing effects of anisotropy on seismic
752 moments and their potency-tensor isotropic equivalent, Geophysics, 83, no. 3, C85–C97,
753 doi: 10.1190/geo2017-0442.1.

754 Bommer, J.J., Oates, S., Cepeda, J.M., Lindholm, C., Bird, J., Torres, R., Marroquín, G. and
755 Rivas, J., 2006. Control of hazard due to seismicity induced by a hot fractured rock
756 geothermal project. Engineering Geology, 83(4), pp.287-306.

757 Breuer, A., A. Heinecke, and M. Bader, 2016, Petascale Local Time Stepping for the ADER-DG
758 Finite Element Method, in Proceedings - 2016 IEEE 30th International Parallel and
759 Distributed Processing Symposium, IPDPS 2016, Institute of Electrical and Electronics
760 Engineers Inc., 854–863.

761 Breuer, A., A. Heinecke, S. Rettenberger, M. Bader, A.-A. Gabriel, and C. Pelties, 2014,
762 Sustained Petascale Performance of Seismic Simulations with SeisSol on SuperMUC, 1–18.

763 Bydlon, S. A., and E. M. Dunham, 2015, Rupture dynamics and ground motions from
764 earthquakes in 2-D heterogeneous media, Geophys. Res. Lett., 42, no. 6, 1701–1709, doi:
765 10.1002/2014GL062982.

766 Cappa, F., and J. Rutqvist, 2012, Seismic rupture and ground accelerations induced by CO 2
767 injection in the shallow crust, Geophys. J. Int., 190, no. 3, 1784–1789, doi: 10.1111/j.1365-
768 246X.2012.05606.x.

769 Chang, K. W., H. Yoon, Y. Kim, and M. Y. Lee, 2020, Operational and geological controls of
770 coupled poroelastic stressing and pore-pressure accumulation along faults: Induced
771 earthquakes in Pohang, South Korea, Sci. Rep., 10, no. 1, 2073, doi: 10.1038/s41598-020-
772 58881-z.

773 Cheng, Y., and X. Chen, 2018, Characteristics of seismicity inside and outside the salton sea
774 geothermal field, Bull. Seismol. Soc. Am., 108, no. 4, 1877–1888, doi:
775 10.1785/0120170311.

776 Choi, J. H. et al., 2019, Surface deformations and rupture processes associated with the 2017 Mw
777 5.4 Pohang, Korea, earthquake, Bull. Seismol. Soc. Am., 109, no. 2, 756–769, doi:
778 10.1785/0120180167.

779 Cornet, F.H., Bérard, T. and Bourouis, S., 2007. How close to failure is a granite rock mass at a 5
780 km depth?. International Journal of Rock Mechanics and Mining Sciences, 44(1), pp.47-66.

781 Cuenot, N., J. Charléty, L. Dorbath, and H. Haessler, 2006, Faulting mechanisms and stress
782 regime at the European HDR site of Soultz-sous-Forêts, France, Geothermics, 35, nos. 5–6,
783 561–575, doi: 10.1016/j.geothermics.2006.11.007.

784 Dieterich, J. H., K. B. Richards-Dinger, and K. A. Kroll, 2015, Modeling injection-induced
785 seismicity with the physics-based earthquake simulator RSQSim, Seismol. Res. Lett., 86,
786 no. 4, 1102–1109, doi: 10.1785/0220150057.

787 Duan, B., 2016, Spontaneous rupture on natural fractures and seismic radiation during hydraulic
788 fracturing treatments, Geophys. Res. Lett., 43, no. 14, 7451–7458, doi:
789 10.1002/2016GL069083.

790 Dumbser, M., and M. Käser, 2006, An arbitrary high-order discontinuous Galerkin method for
791 elastic waves on unstructured meshes - II. The three-dimensional isotropic case, Geophys. J.
792 Int., 167, no. 1, 319–336, doi: 10.1111/j.1365-246X.2006.03120.x.

793 Dunham, E. M., D. Belanger, L. Cong, and J. E. Kozdon, 2011a, Earthquake ruptures with
794 strongly rate-weakening friction and off-fault plasticity, part 1: Planar faults, Bull. Seismol.
795 Soc. Am., 101, no. 5, 2296–2307, doi: 10.1785/0120100075.

796 Dunham, E. M., D. Belanger, L. Cong, and J. E. Kozdon, 2011b, Earthquake ruptures with
797 strongly rate-weakening friction and off-fault plasticity, part 2: Nonplanar faults, Bull.
798 Seismol. Soc. Am., 101, no. 5, 2308–2322, doi: 10.1785/0120100076.

799 Ellsworth, W. L., D. Giardini, J. Townend, S. Ge, and T. Shimamoto, 2019, Triggering of the
800 Pohang, Korea, Earthquake (Mw 5.5) by enhanced geothermal system stimulation,
801 Seismological Society of America, 1844–1858.

802 Emerson paradigm holding, 2018, GoCad: A computer aided design program for geological
803 applications.

804 Gabriel, A.-A., J.-P. Ampuero, L. A. Dalguer, and P. M. Mai, 2013, Source properties of
805 dynamic rupture pulses with off-fault plasticity, J. Geophys. Res. Solid Earth, 118, no. 8,
806 4117–4126, doi: 10.1002/jgrb.50213.

807 Galis, M., J. P. Ampuero, P. M. Mai, and F. Cappa, 2017, Induced seismicity provides insight
808 into why earthquake ruptures stop, Sci. Adv., 3, no. 12, doi: 10.1126/sciadv.aap7528.

809 Gallovič, F., Valentová, Ľ., Ampuero, J.-P., and Gabriel, A.-A. , 2019a. Bayesian dynamic finite-
810 fault inversion: 1. Method and synthetic test. J. Geophys. Res., 124, 6949– 6969.
811 https://doi.org/10.1029/2019JB017510

812 Gallovič, F., Valentová, Ľ., Ampuero, J.-P., and Gabriel, A.-A., 2019b. Bayesian Dynamic
813 Finite-Fault Inversion: 2. Application to the 2016 Mw6.2 Amatrice, Italy, Earthquake, J.
814 Geophys. Res., doi:10.1029/2019JB017512.

815 Garagash, D. I., and L. N. Germanovich, 2012, Nucleation and arrest of dynamic slip on a
816 pressurized fault, J. Geophys. Res. B Solid Earth, 117, no. 10, doi: 10.1029/2012JB009209.

817 Grigoli, F., S. Cesca, A. P. Rinaldi, A. Manconi, J. A. López-Comino, J. F. Clinton, R.
818 Westaway, C. Cauzzi, T. Dahm, and S. Wiemer, 2018, The November 2017 M w 5.5
819 Pohang earthquake: A possible case of induced seismicity in South Korea, Science (80-. ).,
820 360, no. 6392, 1003–1006, doi: 10.1126/science.aat2010.

821 Happ, C., Scheipl, F., Gabriel, A.-A., Greven, S. A general framework for multivariate
822 functional principal component analysis of amplitude and phase variation. Stat. 2019;
823 8:e220. https://doi.org/10.1002/sta4.220

824 Hardebeck, J. L., and A. J. Michael, 2006, Damped regional-scale stress inversions:
825 Methodology and examples for southern California and the Coalinga aftershock sequence,
826 J. Geophys. Res. Solid Earth, 111, no. B11, doi: 10.1029/2005JB004144.

827 Harris, R. A. et al., 2018, A suite of exercises for verifying dynamic earthquake rupture codes,
828 Seismol. Res. Lett., 89, no. 3, 1146–1162, doi: 10.1785/0220170222.

829 Harris, R. A. et al., 2011, Verifying a Computational Method for Predicting Extreme Ground
830 Motion, Seismol. Res. Lett., 82, no. 5, 638–644, doi: 10.1785/gssrl.82.5.638.

831 Heidbach, O. M. Rajabi, X. Cui, K. Fuchs, B. Muller, J. Reinecker, K. Reiter, M. Tingay, F.
832 Wenzel, F. Xie, M. O. Ziegler, M.-L Zoback, M. Zoback, 2018, The World Stress Map
833 database release 2016: Crustal stress pattern across scales, Elsevier B.V., 484–498.

834 Heinecke, A., A. Breuer, S. Retenberger, M. Bader, A.-A. Gabriel, C. Pelties, A. Bode, W.
835 Barth, X. Liao, K. Vaidyanathan, M. Smelyankiy, P. Dubei, 2014, Petascale High Order
836 Dynamic Rupture Earthquake Simulations on Heterogeneous Supercomputers, in
837 International Conference for High Performance Computing, Networking, Storage and
838 Analysis, SC, IEEE Computer Society, 3–14.

839 Hirata, T., 1989, Fractal dimension of fault systems in Japan: Fractal structure in rock fracture
840 geometry at various scales, Pure Appl. Geophys. PAGEOPH, 131, nos. 1–2, 157–170, doi:
841 10.1007/BF00874485.

842 Hofmann, H., G, Zimmermann,M. Farkas, E. Huenges, A. Zang, M. Leonhardt et al., 2019, First
843 field application of cyclic soft stimulation at the Pohang Enhanced Geothermal System site
844 in Korea, Geophys. J. Int. (2019) 217, 926–949

845 Hunter, J. D., 2007, Matplotlib: A 2D graphics environment, Comput. Sci. Eng., 9, no. 3, 99–
846 104, doi: 10.1109/MCSE.2007.55.

847 Jeanne, P., J. Rutqvist, P. F. Dobson, J. Garcia, M. Walters, C. Hartline, and A. Borgia, 2015,
848 Geomechanical simulation of the stress tensor rotation caused by injection of cold water in a
849 deep geothermal reservoir, J. Geophys. Res. Solid Earth, 120, no. 12, 8422–8438, doi:
850 10.1002/2015JB012414.

851 Jin, L., and M. D. Zoback, 2018, Fully Dynamic Spontaneous Rupture Due to Quasi-Static Pore
852 Pressure and Poroelastic Effects: An Implicit Nonlinear Computational Model of Fluid-
853 Induced Seismic Events, J. Geophys. Res. Solid Earth, 123, no. 11, 9430–9468, doi:
854 10.1029/2018JB015669.

855 Julian, B. R., A. D. Miller, and G. R. Foulger, 1998, Non-double-couple earthquakes 1. Theory,
856 Rev. Geophys., 36, no. 4, 525–549, doi: 10.1029/98RG00716.

857 Kang, S., B. Kim, S. Bae, H. Lee, and M. Kim, 2019a, Earthquake-Induced Ground
858 Deformations in the Low-Seismicity Region: A Case of the 2017 M5.4 Pohang, South
859 Korea, Earthquake, Earthq. Spectra, 35, no. 3, 1235–1260, doi: 10.1193/062318EQS160M.

860 Kang, S., B. Kim, H. Cho, J. Lee, K. Kim, S. Bae, and C. Sun, 2019b, Ground-Motion
861 Amplifications in Small-Size Hills: Case Study of Gokgang-ri, South Korea, during the
862 2017 ML 5.4 Pohang Earthquake Sequence, Bull. Seismol. Soc. Am., 109, no. 6, 2626–
863 2643, doi: 10.1785/0120190064.

864 Käser, M., and M. Dumbser, 2006, An arbitrary high-order discontinuous Galerkin method for
865 elastic waves on unstructured meshes - I. The two-dimensional isotropic case with external

source terms, Geophys. J. Int., 166, no. 2, 855–877, doi: 10.1111/j.1365-246X.2006.03051.x.

Kim, K. H., J. H. Ree, Y. H. Kim, S. Kim, S. Y. Kang, and W. Seo, 2018, Assessing whether the 2017 Mw5.4 Pohang earthquake in South Korea was an induced event, Science (80-. )., 360, no. 6392, 1007–1009, doi: 10.1126/science.aat6081.

Kim, K. H., W. Seo, J. Han, J. Kwon, S. Y. Kang, J. H. Ree, S. Kim, and K. Liu, 2020, The 2017 ML 5.4 Pohang earthquake sequence, Korea, recorded by a dense seismic network, Tectonophysics, 774, doi: 10.1016/j.tecto.2019.228306.

Kim, H., L. Xie, K. B. Min, S. Bae, and O. Stephansson, 2017, Integrated In Situ Stress Estimation by Hydraulic Fracturing, Borehole Observations and Numerical Analysis at the EXP-1 Borehole in Pohang, Korea, Rock Mech. Rock Eng., 50, no. 12, 3141–3155, doi: 10.1007/s00603-017-1284-1.

Klinger, Y., K. Okubo, A. Vallage, J. Champenois, A. Delorme, E. Rougier, Z. Lei, E. E. Knight, A. Munjiza, C. Satriano, S. Baize, R. Langridge, H. S. Bhat, 2018, Earthquake Damage Patterns Resolve Complex Rupture Processes, Geophys. Res. Lett., 45, no. 19, 10,279-10,287, doi: 10.1029/2018GL078842.

Korean Government Commission, 2019, Summary Report of the Korean Government Commission on Relations between the 2017 Pohang Earthquake and EGS Project.

Krischer, L., A. R. Hutko, M. Van Driel, S. Stähler, M. Bahavar, C. Trabant, and T. Nissen-Meyer, 2017, On-demand custom broadband synthetic seismograms, Seismol. Res. Lett., 88, no. 4, 1127–1140, doi: 10.1785/0220160210.

Kroll, K. A., K. B. Richards-Dinger, and J. H. Dieterich, 2017, Sensitivity of Induced Seismic Sequences to Rate-and-State Frictional Processes, J. Geophys. Res. Solid Earth, 122, no. 12, 10,207-10,219, doi: 10.1002/2017JB014841.

Kwiatek, G. et al., 2019, Controlling fluid-induced seismicity during a 6.1-km-deep geothermal stimulation in Finland, Sci. Adv., 5, no. 5, eaav7224, doi: 10.1126/sciadv.aav7224.

Kyriakopoulos, C., D. D. Oglesby, T. K. Rockwell, A. J. Meltzner, M. Barall, J. M. Fletcher, and D. Tulanowski, 2019, Dynamic Rupture Scenarios in the Brawley Seismic Zone, Salton Trough, Southern California, J. Geophys. Res. Solid Earth, 124, no. 4, 3680–3707, doi: 10.1029/2018JB016795.

de la Puente, J., J.-P. Ampuero, and M. Käser, 2009, Dynamic rupture modeling on unstructured meshes using a discontinuous Galerkin method, J. Geophys. Res., 114, no. B10, B10302, doi: 10.1029/2008JB006271.

Lee, K. K. et al., 2019, Managing injection-induced seismic risks, Science, 364, no. 6442, 730–732, doi: 10.1126/science.aax1878.

Lee, J., T. K. Hong, and C. Chang, 2017, Crustal stress field perturbations in the continental margin around the Korean Peninsula and Japanese islands, Tectonophysics, 718, 140–149, doi: 10.1016/j.tecto.2017.08.003.

Lee, H., Y. J. Shinn, S. H. Ong, S. W. Woo, K. G. Park, T. J. Lee, and S. W. Moon, 2017, Fault reactivation potential of an offshore CO2 storage site, Pohang Basin, South Korea, J. Pet. Sci. Eng., 152, 427–442, doi: 10.1016/j.petrol.2017.03.014.

907 Liu, J. and Zahradník, J., The 2019 MW 5.7 Changning earthquake, Sichuan Basin, China–a
908 shallow doublet with different faulting styles. Geophys. Res. Let., p.e2019GL085408.

909 Ma, S., 2008, A physical model for widespread near-surface and fault zone damage induced by
910 earthquakes. *Geochemistry, Geophysics, Geosystems*, *9*(11).

911 Mai, P. M., M. Galis, K. K. S. Thingbaijam, J. C. Vyas, and E. M. Dunham, 2018, Accounting
912 for Fault Roughness in Pseudo-Dynamic Ground-Motion Simulations, Birkhäuser, Cham,
913 95–126.

914 Martínez-Garzón, P., M. Bohnhoff, G. Kwiatek, and G. Dresen, 2013, Stress tensor changes
915 related to fluid injection at The Geysers geothermal field, California, Geophys. Res. Lett.,
916 40, no. 11, 2596–2601, doi: 10.1002/grl.50438.

917 Martínez-Garzón, P., G. Kwiatek, H. Sone, M. Bohnhoff, G. Dresen, and C. Hartline, 2014,
918 Spatiotemporal changes, faulting regimes, and source parameters of induced seismicity: A
919 case study from The Geysers geothermal field, J. Geophys. Res. Solid Earth, 119, no. 11,
920 8378–8396, doi: 10.1002/2014JB011385.

921 McGarr, A., 2014, Maximum magnitude earthquakes induced by fluid injection, J. Geophys.
922 Res. Solid Earth, 119, no. 2, 1008–1019, doi: 10.1002/2013JB010597.

923 Mignan, A., Landtwing, D., Kästli, P., Mena, B. and Wiemer, S., 2015. Induced seismicity risk
924 analysis of the 2006 Basel, Switzerland, Enhanced Geothermal System project: Influence of
925 uncertainties on risk mitigation. *Geothermics*, *53*, pp.133-146.

926 Okubo, K., H. S. Bhat, E. Rougier, S. Marty, A. Schubnel, Z. Lei, E. E. Knight, and Y. Klinger,

2019, Dynamics, Radiation, and Overall Energy Budget of Earthquake Rupture With Coseismic Off-Fault Damage, J. Geophys. Res. Solid Earth, 124, no. 11, 11771–11801, doi: 10.1029/2019JB017304.

Pelties, C., A.-A. Gabriel, and J.-P. Ampuero, 2014, Verification of an ADER-DG method for complex dynamic rupture problems, Geosci. Model Dev., 7, no. 3, 847–866, doi: 10.5194/gmd-7-847-2014 and Geoscientific Model Development Discussions, 6(4), 5981--6034, doi:10.5194/gmdd-6-5981-2013.

Pelties, C., Y. Huang, and J. P. Ampuero, 2015, Pulse-Like Rupture Induced by Three-Dimensional Fault Zone Flower Structures, Pure Appl. Geophys., 172, no. 5, 1229–1241, doi: 10.1007/s00024-014-0881-0.

Pelties, C., J. de la Puente, J.-P. Ampuero, G. B. Brietzke, and M. Käser, 2012, Three-dimensional dynamic rupture simulation with a high-order discontinuous Galerkin method on unstructured tetrahedral meshes, J. Geophys. Res. Solid Earth, 117, no. B2, n/a-n/a, doi: 10.1029/2011JB008857.

Peyrat, S., K. Olsen, and R. Madariaga, 2001, Dynamic modeling of the 1992 Landers earthquake, J. Geophys. Res. Solid Earth, 106, no. B11, 26467–26482, doi: 10.1029/2001jb000205.

Rettenberger, S., O. Meister, M. Bader, and A. A. Gabriely, 2016, ASAGI - A parallel server for adaptive geoinformation, in ACM International Conference Proceeding Series, Association for Computing Machinery.

Richards-Dinger, K., and J. H. Dieterich, 2012, RSQSim earthquake simulator, Seismol. Res.

948 Lett., 83, no. 6, 983–990, doi: 10.1785/0220120105.

949 Ripperger, J., Mai, P.M. and Ampuero, J.P., 2008. Variability of near-field ground motion from
950 dynamic earthquake rupture simulations. *Bulletin of the seismological society of America*,
951 *98*(3), pp.1207-1228.

952 Roten, D., K. B. Olsen, S. M. Day, Y. Cui, and D. Fäh, 2014, Expected seismic shaking in Los
953 Angeles reduced by San Andreas fault zone plasticity, Geophys. Res. Lett., 41, no. 8, 2769–
954 2777, doi: 10.1002/2014GL059411.

955 Schoenball, M., L. Dorbath, E. Gaucher, J. F. Wellmann, and T. Kohl, 2014, Change of stress
956 regime during geothermal reservoir stimulation, Geophys. Res. Lett., 41, no. 4, 1163–1170,
957 doi: 10.1002/2013GL058514.

958 Schoenball, M., T. M. Müller, B. I. R. Müller, and O. Heidbach, 2010, Fluid-induced
959 microseismicity in pre-stressed rock masses, Geophys. J. Int., 180, no. 2, 813–819, doi:
960 10.1111/j.1365-246X.2009.04443.x.

961 Shi, Z., and S. M. Day, 2013, Rupture dynamics and ground motion from 3-D rough-fault
962 simulations, J. Geophys. Res. Solid Earth, 118, no. 3, 1122–1141, doi: 10.1002/jgrb.50094.

963 Simmetrix Inc, 2017, SimModeler: Simulation modeling suite 14.0 documentation (Tech. Rep.).

964 Soh, I., C. Chang, J. Lee, T.-K. Hong, and E.-S. Park, 2018, Tectonic stress orientations and
965 magnitudes, and friction of faults, deduced from earthquake focal mechanism inversions
966 over the Korean Peninsula, Geophys. J. Int., 213, no. 2, 1360–1373, doi:
967 10.1093/gji/ggy061.

968 Song, S. G., and H. Lee, 2019, Static slip model of the 2017 M w 5.4 Pohang, South Korea,
969 earthquake constrained by the InSAR data, Seismol. Res. Lett., 90, no. 1, 140–148, doi:
970 10.1785/0220180156.

971 Di Toro, G., R. Han, T. Hirose, N. De Paola, S. Nielsen, K. Mizoguchi, F. Ferri, M. Cocco, and
972 T. Shimamoto, 2011, Fault lubrication during earthquakes, Nature, 471, no. 7339, 494–499,
973 doi: 10.1038/nature09838.

974 Taufiqurrahman, T., A.-A. Gabriel, B. Li, D. Li, S. A. Wirp, T. Ulrich, K. H. Palgunadi, A.
975 Verdecchia, S. Carena, and Z. K. Mildon, 2019, High-resolution integrated dynamic rupture
976 modeling of the 2019 M6. 4 Searles Valley and M7. 1 Ridgecrest earthquakes. S31G-0487
977 presented at 2019 Fall Meeting, AGU, San Francisco, CA, 9-13 Dec.

978 Templeton, E.L. and Rice, J.R., 2008. Off-fault plasticity and earthquake rupture dynamics: 1.
979 Dry materials or neglect of fluid pressure changes. J. Geophys. Res.: Solid Earth, 113(B9).

980 Ulrich, T., and A.-A. Gabriel, 2017, 3D fault curvature and fractal roughness: Insights for
981 rupture dynamics and ground motions using a Discontinuous Galerkin method. In EGU
982 General Assembly Conference Abstract, Vol. 19, Vienna, Austria, pp. 18689.

983 Ulrich, Thomas, A. A. Gabriel, J. P. Ampuero, and W. Xu, 2019a, Dynamic viability of the 2016
984 Mw 7.8 Kaikōura earthquake cascade on weak crustal faults, Nat. Commun., 10, no. 1, doi:
985 10.1038/s41467-019-09125-w.

986 Ulrich, T., S. Vater, E. H. Madden, J. Behrens, Y. van Dinther, I. van Zelst, E. J. Fielding, C.
987 Liang, and A. A. Gabriel, 2019b, Coupled, Physics-Based Modeling Reveals Earthquake
988 Displacements are Critical to the 2018 Palu, Sulawesi Tsunami, Pure Appl. Geophys., 176,

989 no. 10, 4069–4109, doi: 10.1007/s00024-019-02290-5.

990 Uphoff, C. and Bader, M., 2016, July. Generating high performance matrix kernels for
991 earthquake simulations with viscoelastic attenuation. In 2016 International Conference on
992 High Performance Computing and Simulation (HPCS) (pp. 908-916). IEEE.

993 Uphoff, C., S. Rettenberger, M. Bader, E. H. Madden, T. Ulrich, S. Wollherr, and A.-A. Gabriel,
994 2017, Extreme scale multi-physics simulations of the tsunamigenic 2004 sumatra
995 megathrust earthquake, Proc. Int. Conf. High Perform. Comput. Networking, Storage Anal.
996 - SC '17, no. November, 1–16, doi: 10.1145/3126908.3126948.

997 Vavryčuk, V., 2015, Moment tensor decompositions revisited, J. Seismol., 19, no. 1, 231–252,
998 doi: 10.1007/s10950-014-9463-y.

999 Viesca, R. C., and J. R. Rice, 2012, Nucleation of slip-weakening rupture instability in landslides
1000 by localized increase of pore pressure, J. Geophys. Res. Solid Earth, 117, no. 3, doi:
1001 10.1029/2011JB008866.

1002 Wang, Y., G. Ouillon, J. Woessner, D. Sornette, and S. Husen, 2013, Automatic reconstruction
1003 of fault networks from seismicity catalogs including location uncertainty, J. Geophys. Res.
1004 Solid Earth, 118, no. 11, 5956–5975, doi: 10.1002/2013JB010164.

1005 Wessel, P., W. H. F. Smith, R. Scharroo, J. Luis, and F. Wobbe, 2013, Generic Mapping Tools:
1006 Improved Version Released, Eos, Trans. Am. Geophys. Union, 94, no. 45, 409–410, doi:
1007 10.1002/2013EO450001.

1008 Wolf, Sebastian, A.-A. Gabriel, and M. Bader (2020), Optimisation and Local Time Stepping of

an ADER-DG Scheme for Fully Anisotropic Wave Propagation in Complex Geometries, in Proceedings of the 10th International Workshop on Advances in High-Performance Computational Earth Sciences: Applications and Frameworks, preprint available at https://wolke.geophysik.uni-muenchen.de/s/ReaBg7mjabPwwLk#pdfviewer.

Wollherr, S., A. Gabriel, and P. M. Mai, 2019, Landers 1992 "Reloaded": Integrative Dynamic Earthquake Rupture Modeling, J. Geophys. Res. Solid Earth, 124, no. 7, 6666–6702, doi: 10.1029/2018JB016355.

Wollherr, S., A. A. Gabriel, and C. Uphoff, 2018, Off-fault plasticity in three-dimensional dynamic rupture simulations using a modal Discontinuous Galerkin method on unstructured meshes: Implementation, verification and application, Geophys. J. Int., 214, no. 3, 1556–1584, doi: 10.1093/GJI/GGY213.

Woo, J. -U., M. Kim, D. -H. Sheen, T. -S. Kang, J. Rhie, F. Grigoli, W. L. Ellsworth, and D. Giardini, 2019, An In-Depth Seismological Analysis Revealing a Causal Link Between the 2017 M $_W$ 5.5 Pohang Earthquake and EGS Project, J. Geophys. Res. Solid Earth, 2019JB018368, doi: 10.1029/2019JB018368.

Yamashita, T., and Y. Umeda, 1994, Earthquake rupture complexity due to dynamic nucleation and interaction of subsidiary faults, Pure Appl. Geophys. PAGEOPH, 143, nos. 1–3, 89–116, doi: 10.1007/BF00874325.

Zaliapin, I., and Y. Ben-Zion, 2013, Earthquake clusters in southern California I: Identification and stability, J. Geophys. Res. Solid Earth, 118, no. 6, 2847–2864, doi: 10.1002/jgrb.50179.

van Zelst, I., S. Wollherr, A. -A. Gabriel, E. H. Madden, and Y. Dinther, 2019, Modeling

Megathrust Earthquakes Across Scales: One-way Coupling From Geodynamics and Seismic Cycles to Dynamic Rupture, J. Geophys. Res. Solid Earth, 124, no. 11, 11414–11446, doi: 10.1029/2019JB017539.

Zhan, Z., 2019, Distributed acoustic sensing turns fiber-optic cables into sensitive seismic antennas, Seismol. Res. Lett., 91, no. 1, 1–15, doi: 10.1785/0220190112.

Zhang, Q., and P. M. Shearer, 2016, A new method to identify earthquake swarms applied to seismicity near the San Jacinto Fault, California, Geophys. J. Int., 205, no. 2, 995–1005, doi: 10.1093/gji/ggw073.

Ziegler, M. O., O. Heidbach, A. Zang, P. Martínez-Garzón, and M. Bohnhoff, 2017, Estimation of the differential stress from the stress rotation angle in low permeable rock, Geophys. Res. Lett., 44, no. 13, 6761–6770, doi: 10.1002/2017GL073598.

**FULL AUTHOR'S MAILING LIST**

Kadek Hendrawan Palgunadi : kadek.palgunadi@kaust.edu.sa

Alice-Agnes Gabriel : gabriel@geophysik.uni-muenchen.de

Thomas Ulrich : ulrich@geophysik.uni-muenchen.de

José Ángel López-Comino : lopezcomino@uni-potsdam.de

Paul Martin Mai : martin.mai@kaust.edu.sa

**TABLES:**

**Table 1**. *Fault friction parameters assumed in this study*

| Parameter | Symbol | Value |
|---|---|---|
| Direct effect parameter | $a$ | 0.01 - 0.02 for z≤3.3 km and 0.01 for z > 3.3 km |
| Evolution effect parameter | $b$ | 0.014 |
| Reference slip velocity | $V_0$ | $10^{-6}$m/s |
| Steady-state friction coefficient at $V_0$ | $f_0$ | 0.6 |
| State-evolution distance | $L$ | 0.2 m |
| Weakening slip velocity | $V_W$ | 0.1 - 1.0 for z≤3.3 km and 0.1 for z > 3.3 km |
| Fully weakened friction coefficient | $f_W$ | 0.1 |
| Initial slip rate | $V_{ini}$ | $10^{-16}$m/s |



**LIST OF FIGURE CAPTIONS:**

**Figure 1.** Map of the South Korean Peninsula showing the near-regional broadband stations (blue triangles). Solid and dashed lines represent the Yangsan and interpreted geological faults near the Pohang EGS site, respectively. The two inset plots present the location and geometry of the faults of Model 1F (upper panel) and Model 2F (lower panel). The thicker black lines mark the near-surface edge of the fault planes. Colored dots depict aftershocks locations extracted from Kim et al. (2018). The non-double-couple solution of Grigoli et al. (2018) is also shown.

**Figure 2**. Fault reconstruction using guided anisotropic location uncertainty distribution (g-ACLUD). a) Spatiotemporal density plot of the mainshock and aftershocks based on the nearest-neighbor distance. b), c) and d) Two fault plane geometry inferred by the g-ACLUD method. The main fault plane has a strike of 214° and dips at 65°, while the secondary fault plane has a strike 199° and dips at 60°. Black dots depict the seismicity used in this study. The geometry of the faults is shown in views b) as view from North, in c) as view from South, and d) in map view. The red star denotes the hypocenter of the Pohang earthquake.

**Figure 3**. 3D rendering of the unstructured tetrahedral computational mesh, and the fault plane with final slip on the 2 fault preferred model (Model 2F) of the Pohang earthquake (warm colors, in m), and the radiated seismic wavefield 5 seconds after rupture initiation (cold colors, absolute particle velocity in m/s). Note the strong effect of the high-resolution topography on modulating the seismic wavefield.

**Figure 4**. Graphical summary of the outcome of 180 dynamic rupture simulations assuming different combinations of initial relative prestress ratio ($R_0$), fluid-pressure ratio ($\gamma$) and direction of $S_{Hmax}$. The corresponding 180 square frames are filled with color if the combination of parameters is able to trigger self-sustained rupture beyond the nucleation region on any fault. The $S_{Hmax}$ direction is indicated by the size of the frame, leading to six imbricated frames for each set of prestress and fluid-pressure ratio parameters.

**Figure 5**. Overview of the simulated earthquake rupture of the preferred model (Model 2F), showing in a) and b) the space-time evolutions of the absolute slip-rate (in m/s) across the main and secondary fault plane. a) (left panel) view from North displaying the main fault rupture. Snapshots every 0.1 s. (right panel) view from South highlighting the rupture of a portion of the secondary fault. Snapshots every 0.05 s. b-c) Rupture-time contours at intervals of 0.2 s.

**Figure 6**. Distribution of absolute fault slip (in m) in a) and b), and rake angles (in degrees) in c) and d) for the preferred dynamic rupture scenario (Model 2F) a) and c) view from North highlighting the main fault rupture. b) and d) view from South highlighting the rupture of a portion of the secondary fault. The white star in panel a) marks the considered hypocenter location.

**Figure 7**. Moment rate release of a) Model 1F and b) Model 2F and moment tensor representation of the preferred one-fault c) and two-fault d) models.

**Figure 8**. Comparison of synthetic and observed ground motion waveforms. a) Distribution of virtual stations (green triangles) at which synthetic waveforms are compared in b). The beachball is the moment tensor representation of the preferred 2 planes model scenario (Model 2F). Solid and dashed red lines represent the mapped Yangsan fault surface trace and the interpreted fault traces near the Pohang EGS site, respectively. The two rectangles show the location and geometry of the faults used in this study. b) Comparison of synthetic waveforms using one (Model 1F, blue dashed lines) and two fault planes (Model 2F, red solid lines) at the 19 dummy stations located in a). A 0.1 - 2 Hz $4^{th}$order Butterworth filter is applied to all traces. All traces are normalized. For each trace, the maximum velocity amplitude (in m/s) of Model 1F is indicated within a black

square. c) Observed (black) and synthetic (red) waveforms for five regional stations for up-down (UD), east-west (EW) and north-south (NS) components (all located in South Korea, see blue triangles in Figure 1. t = 0 s denotes the origin time of the Pohang earthquake. A 0.033-0.08 Hz $4^{th}$ order Butterworth filter is applied to all traces. Synthetic regional waveforms are generated from the preferred dynamic rupture scenario Model 2F using Instaseis (Krischer et al., 2017) and 2 s accurate Green's functions based on the PREM anisotropic model.

**Figure 9**. ((a) and (b)) Co-seismic surface displacements in the InSAR Line-of-sight (LoS) direction (in m) generated by a) Model 1F; one-plane (rectangle) and b) Model 2F; two-planes (two rectangles) preferred dynamic rupture scenario, respectively. The dashed red lines represent the traces of the interpreted faults near the EGS site.

**FIGURES:**

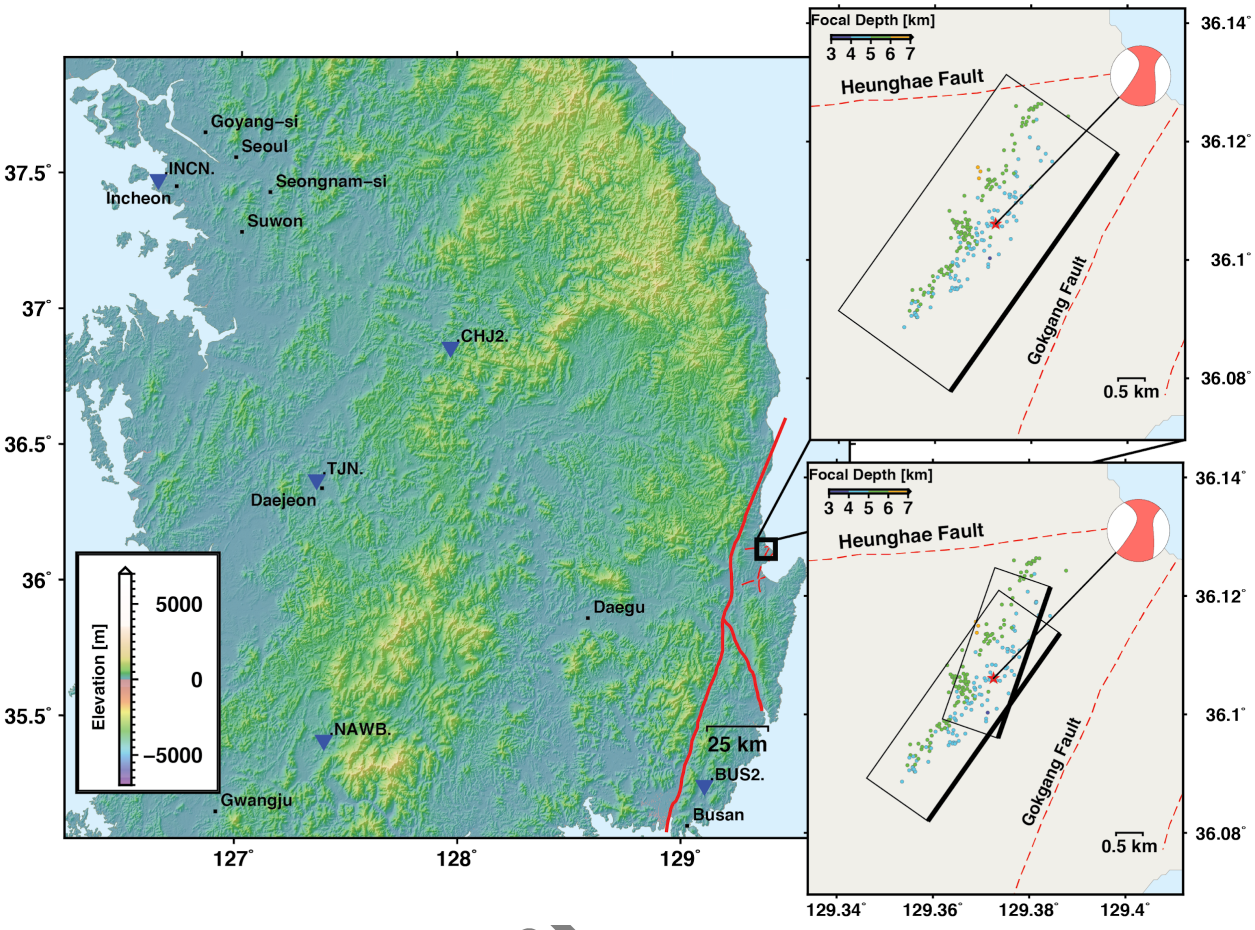


**Figure 1.** Map of the South Korean Peninsula showing the near-regional broadband stations (blue triangles). Solid and dashed lines represent the Yangsan and interpreted geological faults near the Pohang EGS site, respectively. The two inset plots present the location and geometry of the faults of Model 1F (upper panel) and Model 2F (lower panel). The thicker black lines mark the near-surface edge of the fault planes. Colored dots depict aftershocks locations extracted from Kim et al. (2018). The non-double-couple solution of Grigoli et al. (2018) is also shown.

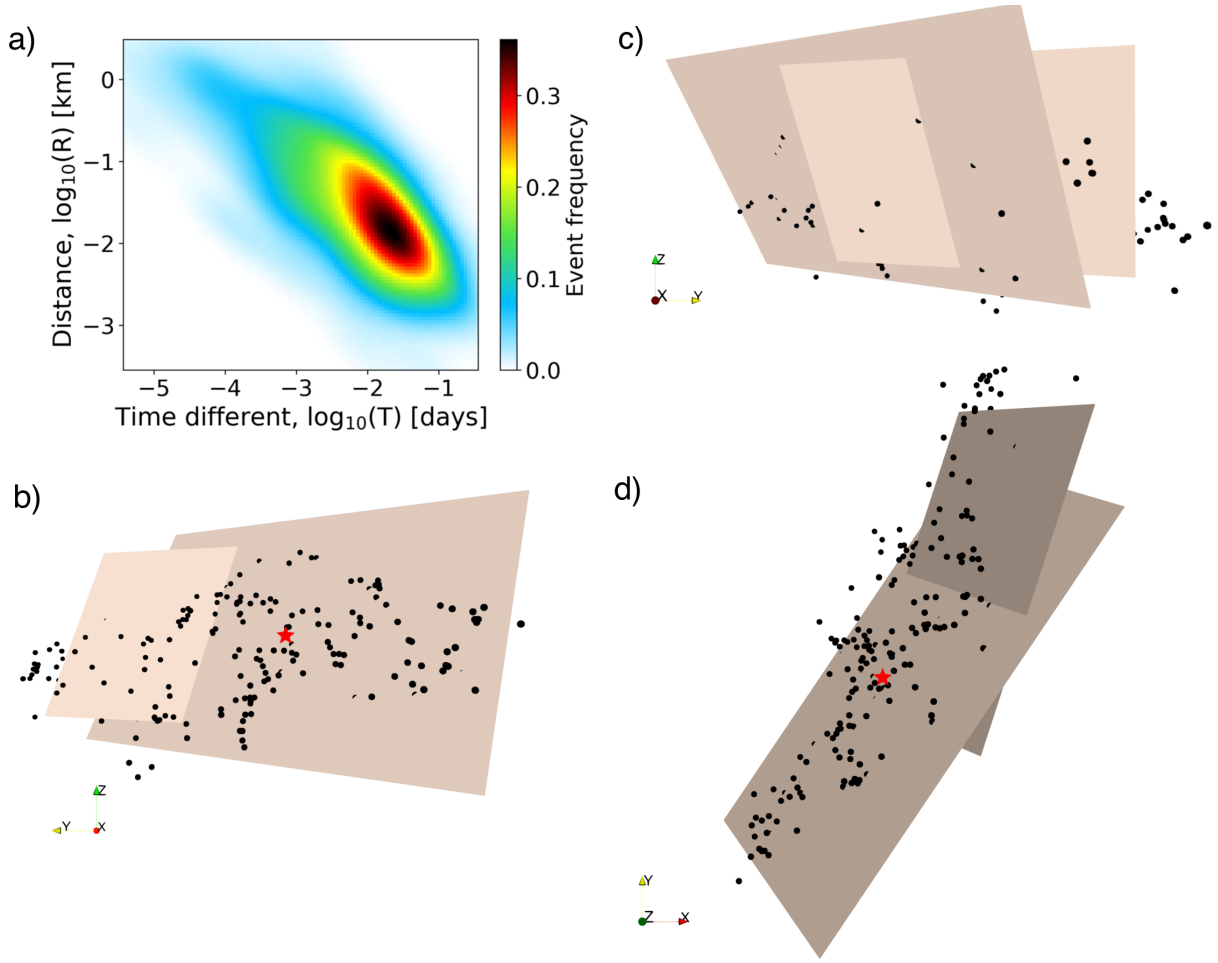


**Figure 2**. Fault reconstruction using guided anisotropic location uncertainty distribution (g-ACLUD). a) Spatiotemporal density plot of the mainshock and aftershocks based on the nearest-neighbor distance. b), c) and d) Two fault plane geometry inferred by the g-ACLUD method. The main fault plane has a strike of 214° and dips at 65°, while the secondary fault plane has a strike 199° and dips at 60°. Black dots depict the seismicity used in this study. The geometry of the faults is shown in views b) as view from North, in c) as view from South, and d) in map view. The red star denotes the hypocenter of the Pohang earthquake.

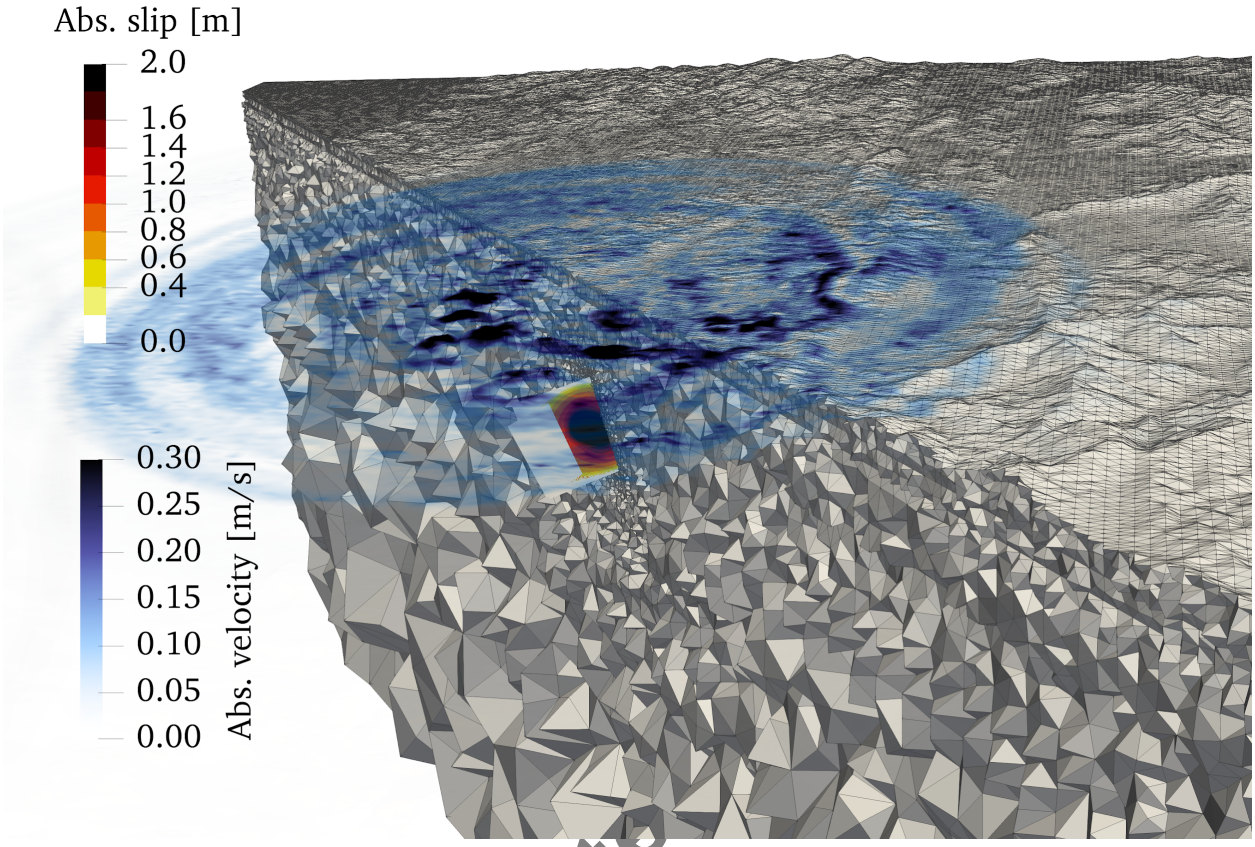


**Figure 3**. 3D rendering of the unstructured tetrahedral computational mesh, and the fault plane with final slip on the 2-fault preferred model (Model 2F) of the Pohang earthquake (warm colors, in m), and the radiated seismic wavefield 5 seconds after rupture initiation (cold colors, absolute particle velocity in m/s). Note the strong effect of the high-resolution topography on modulating the seismic wavefield.

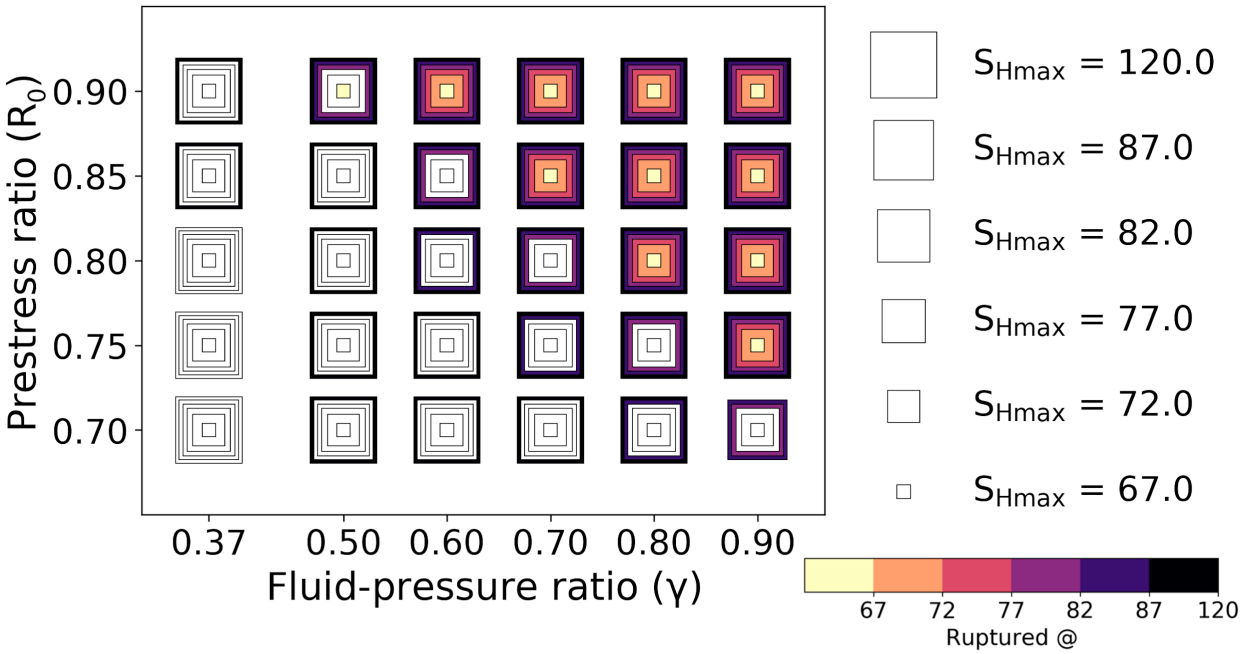


**Figure 4**. Graphical summary of the outcome of 180 dynamic rupture simulations assuming different combinations of initial relative prestress ratio ($R_0$), fluid-pressure ratio ($\gamma$) and direction of $S_{Hmax}$. The corresponding 180 square frames are filled with color if the combination of parameters is able to trigger self-sustained rupture beyond the nucleation region on any fault. The $S_{Hmax}$ direction is indicated by the size of the frame, leading to six imbricated frames for each set of prestress and fluid-pressure ratio parameters.

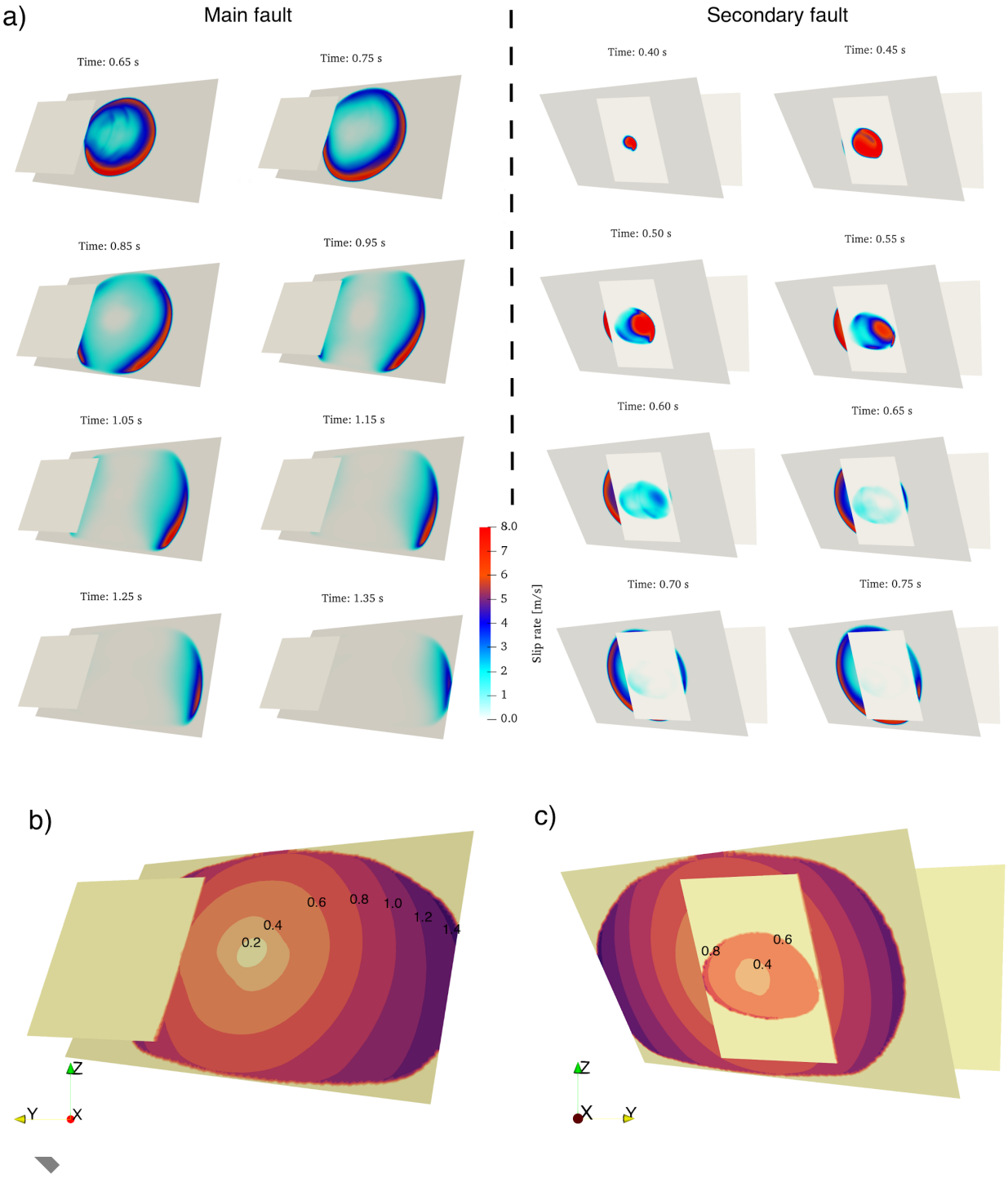


**Figure 5**. Overview of the simulated earthquake rupture of the preferred model (Model 2F), showing in a) and b) the space-time evolutions of the absolute slip-rate (in m/s) across the main and secondary fault plane. a) (left panel) view from North displaying the main fault rupture.

1158 Snapshots every 0.1 s. (right panel) view from South highlighting the rupture of a portion of the
1159 secondary fault. Snapshots every 0.05 s. b-c) Rupture-time contours at intervals of 0.2 s.
1160

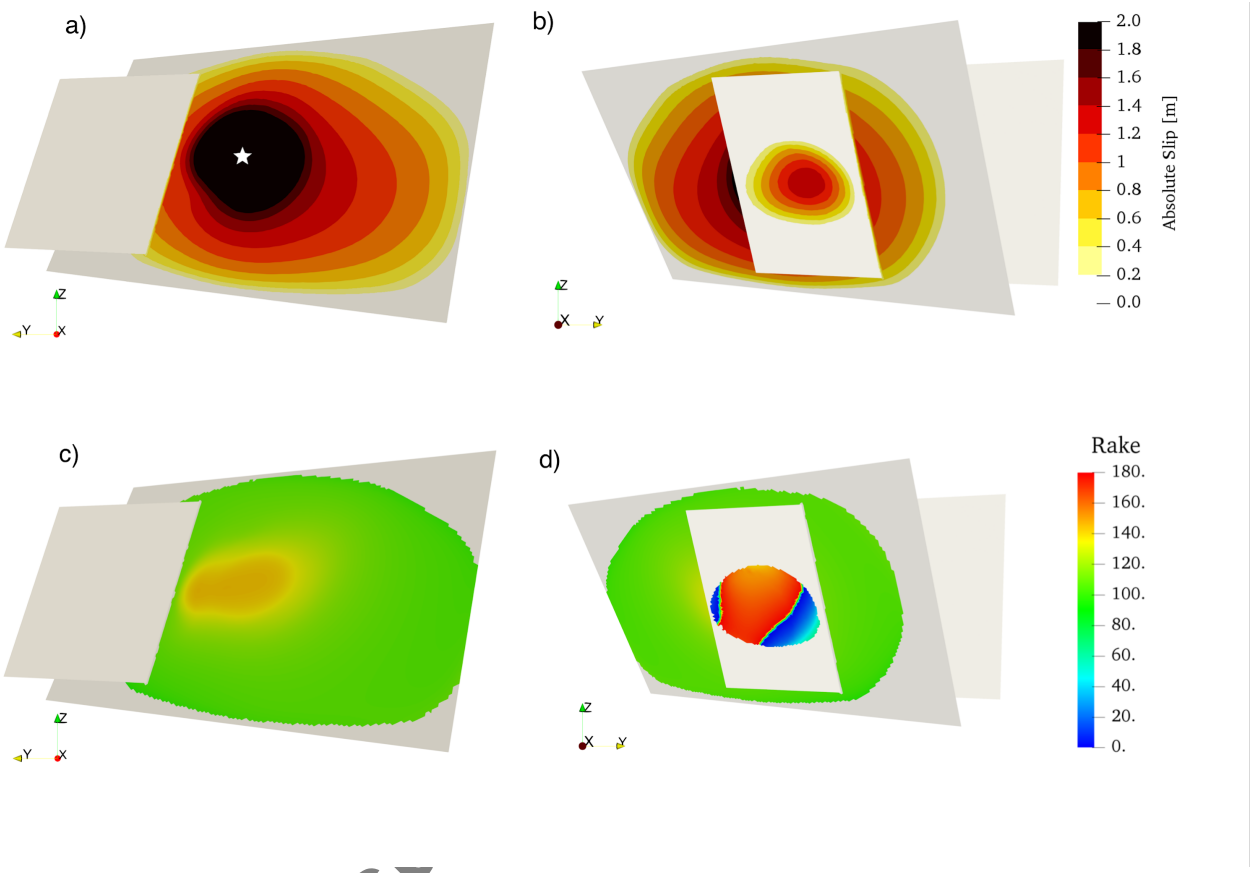


1161
1162 **Figure 6**. Distribution of absolute fault slip (in m) in a) and b), and rake angles (in degrees) in c)
1163 and d) for the preferred dynamic rupture scenario (Model 2F) a) and c) view from North
1164 highlighting the main fault rupture. b) and d) view from South highlighting the rupture of a portion
1165 of the secondary fault. The white star in panel a) marks the considered hypocenter location.
1166
1167
1168
1169

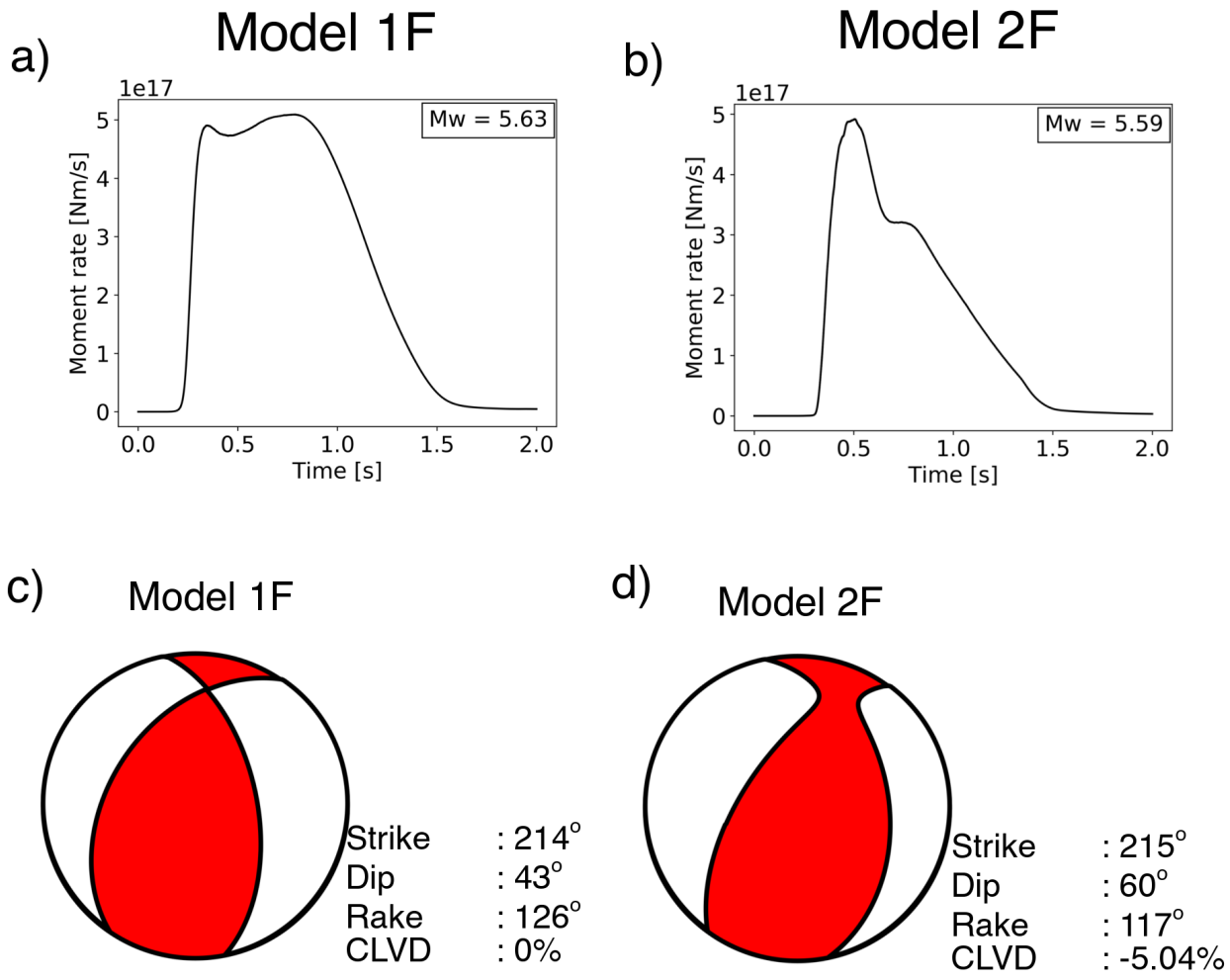


**Figure 7**. Moment rate release of a) Model 1F and b) Model 2F and moment tensor representation of the preferred one-fault c) and two-fault d) models.

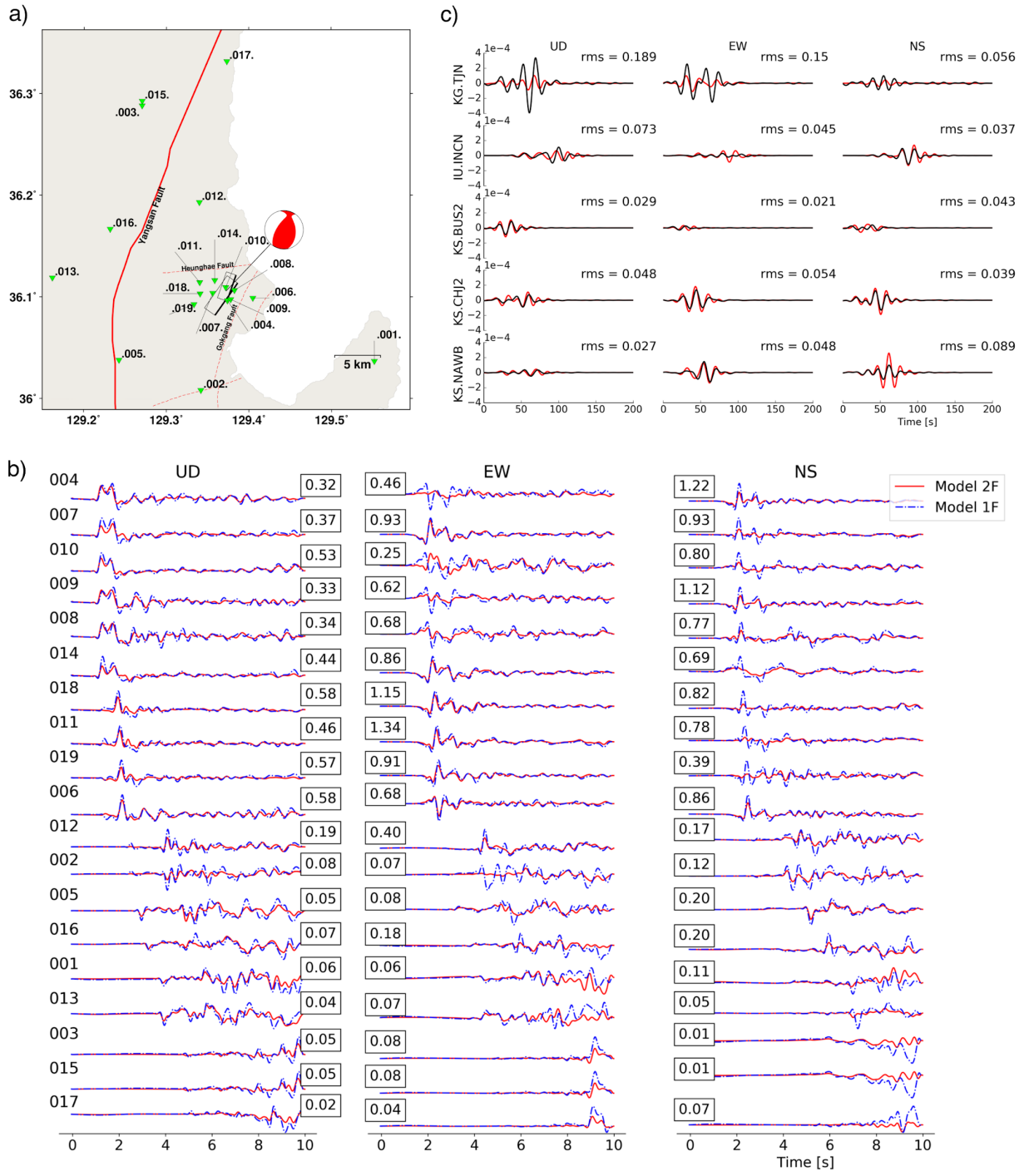


**Figure 8**. Comparison of synthetic and observed ground motion waveforms. a) Distribution of virtual stations (green triangles) at which synthetic waveforms are compared in b). The beachball is the moment tensor representation of the preferred 2 planes model scenario (Model 2F). Solid

and dashed red lines represent the mapped Yangsan fault surface trace and the interpreted fault traces near the Pohang EGS site, respectively. The two rectangles show the location and geometry of the faults used in this study. b) Comparison of synthetic waveforms using one (Model 1F, blue dashed lines) and two fault planes (Model 2F, red solid lines) at the 19 dummy stations located in a). A 0.1 - 2 Hz $4^{th}$order Butterworth filter is applied to all traces. All traces are normalized. For each trace, the maximum velocity amplitude (in m/s) of Model 1F is indicated within a black square. c) Observed (black) and synthetic (red) waveforms for five regional stations for up-down (UD), east-west (EW) and north-south (NS) components (all located in South Korea, see blue triangles in Figure 1. t = 0 s denotes the origin time of the Pohang earthquake. A 0.033-0.08 Hz $4^{th}$ order Butterworth filter is applied to all traces. Synthetic regional waveforms are generated from the preferred dynamic rupture scenario Model 2F using Instaseis (Krischer et al., 2017) and 2 s accurate Green's functions based on the PREM anisotropic model.



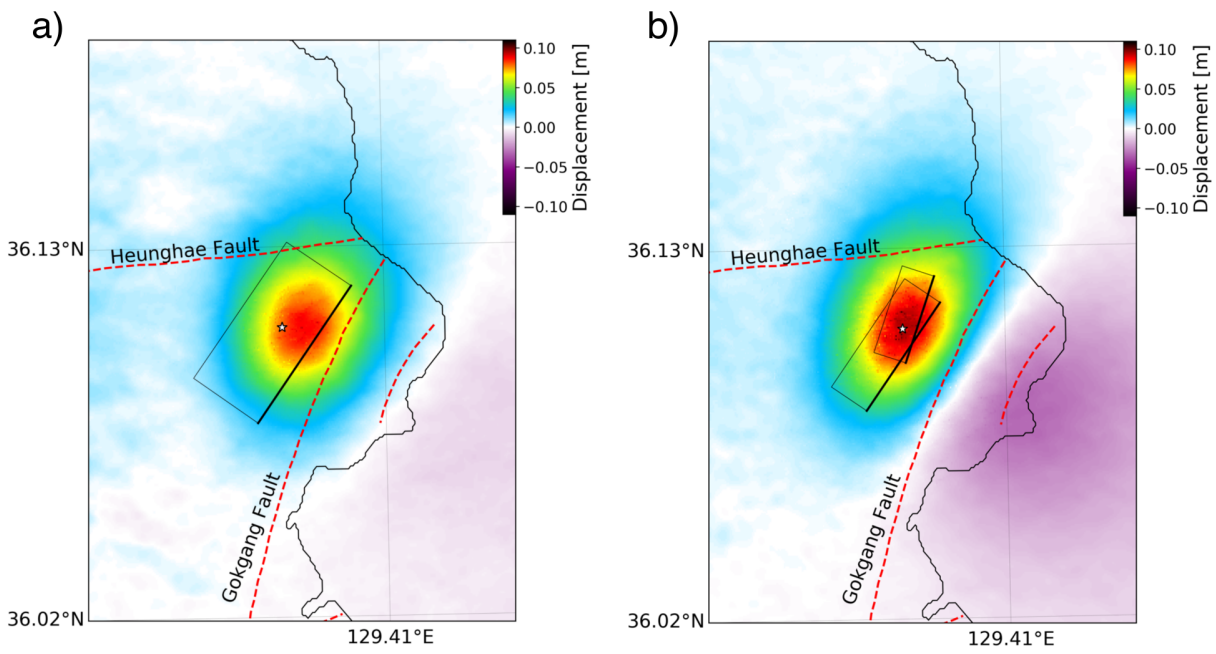

**Figure 9**. ((a) and (b)) Co-seismic surface displacements in the InSAR Line-of-sight (LoS) direction (in m) generated by a) Model 1F; one-plane (rectangle) and b) Model 2F; two-planes (two rectangles) preferred dynamic rupture scenario, respectively. The dashed red lines represent the traces of the interpreted faults near the EGS site.

**APPENDIX**

## A1 Friction parameters

To parameterize the frictional behavior, we use laboratory-based rapid velocity weakening friction law proposed by the community benchmark problem TPV104 Southern California Earthquake Center (SCEC-benchmark) (Harris et al., 2018). The friction law is adapted from - the formulation introduced by Dunham et al. (2011a). The governing equations in our notation are described in Ulrich et al. (2019a), the implementation in SeisSol is described and verified in Pelties et al. (2014). Figure S1b shows the depth-dependent direct effect $a$ and weakening slip velocity $V_W$. The evolution effect parameter $b$ is set constant. We apply a velocity strengthening zone at the top 200 m of all faults to smoothly stop rupture. Within this zone, values for $a$ and $V_W$ increase linearly ranging from 0.01 and 0.1 m/s below depth of 3.3 km to 0.02 and 1.0 m/s to the surface, respectively. Table 1 lists all friction parameters used in this study.

**Table 1**. *Fault friction parameters assumed in this study*

| Parameter | Symbol | Value |
|---|---|---|
| Direct effect parameter | $a$ | 0.01 - 0.02 z≤3.3 km and<br>0.01 z > 3.3 km |

| | | |
|---|---|---|
| Evolution effect parameter | $b$ | 0.014 |
| Reference slip velocity | $V_0$ | $10^{-6}$m/s |
| Steady-state friction coefficient at $V_0$ | $f_0$ | 0.6 |
| State-evolution distance | $L$ | 0.2 m |
| Weakening slip velocity | $V_W$ | 0.1 - 1.0 z≤3.3 km and 0.1 z > 3.3 km |
| Fully weakened friction coefficient | $f_W$ | 0.1 |
| Initial slip rate | $V_{ini}$ | $10^{-16}$m/s |

## A2 Nucleation procedure

To nucleate the earthquake, we apply a time-dependent overstress centered at the hypocenter location, that is at longitude and latitude of 129.37° and 36.11°, respectively, and at a depth of 4.27 km. The time-dependent overstressed nucleation area $R_{nuc}(t)$ is determined by increasing the initial relative prestress ratio $R_0$ as:

$$R_{nuc}(t) = R_0 + \Omega(r) \times S(t) \quad \text{(A2.1)}$$

where $\Omega(r)$ is a Gaussian-step function, $r$ is the radius from the hypocenter, and $S(t)$ denotes the smoothed step function. The Gaussian-step function is defined as:

$$\Omega(r) = \xi\, exp(\frac{r^2}{r^2 - {r_c}^2}) \quad \text{for r} < r_c\ ; \qquad \Omega(r) = 0 \quad \text{otherwise} \qquad \text{(A2.2)}$$

where $\xi$ is the overstressed initial relative prestress ratio and $r_c = 500$ m is the radius of the nucleation patch. We only overstress the main fault plane; In the nucleation region, we set $\xi$ to 2, and apply an overstress characterized by $S_{Hmax}$= 77° and $v = 0.1$. These values are set by trial-and-error to allow rupture to propagate spontaneously with the least magnitude of overstress and to limit fault slip inside the nucleation patch. The orientation of $S_{Hmax}$ is also in accordance with Korean Government Commission, 2019 and Ellsworth et al. (2019) which suggest optimally oriented stress orientation and critically stressed inside the nucleation zone. The smoothed step function is formulated as:

$$S(t) = exp(\frac{(t-T)^2}{t \times (t-2 \times T)}) \quad \text{for } 0 < t < T;\ S(t) = 1 \quad \text{for } t \geq T \qquad \text{(A2.3)}$$

where $T = 0.4$ s is the nucleation time.

## A3 Methodology

### A3.1 Numerical method

We use the open-source software SeisSol (Dumbser and Käser, 2006; Pelties et al., 2014; Uphoff et al., 2017; Wollherr et al., 2018) (https://github.com/SeisSol/SeisSol), which couples seismic wave propagation in complex media and frictional fault failure. SeisSol uses an Arbitrary high-order DERivative-Discontinuous Galerkin (ADER-DG) approach which achieves high-order accuracy in space and time (Käser and Dumbser, 2006). SeisSol uses flexible non-uniform

unstructured tetrahedral mesh, which allows accounting for complex geometric features such as 3D fault networks or high-resolution topography across a large range of scales: from small-scale fault roughness, large-scale fault structures to fault-to-fault interaction. Dynamic rupture simulations are sensitive to geometrically complexity of faults (Dunham et al., 2011b; Shi and Day, 2013; Uphoff et al., 2017; Wollherr et al., 2018, 2019; Ulrich et al., 2019a, 2019b).

A high resolution and accurate simulation are essential to resolve the detailed processes of rupture propagation of the intersected fault geometry. We motivate the presented deterministic parameter study with the computational feasibility of many such simulations. While the feasibility of dynamic rupture inversion and statistical learning approaches has been demonstrated (e.g. Peyrat et al. 2001; Bauer et al., 2018, Happ et al. 2019, Gallovič et al. 2019a, Gallovič et al. 2019b), these are restricted by near-field data availability and the computational cost of each forward dynamic rupture model.

SeisSol is verified in a wide range of benchmark problems, including dipping faults, branched and curved faults, on-fault heterogeneity, and laboratory-based friction laws (de la Puente et al., 2009; Pelties et al., 2012; Pelties et al., 2014; Wollherr et al., 2018,) in line with the SCEC-Benchmark Dynamic Rupture code verification exercises (Harris et al., 2011; Harris et al., 2018) as well as against analytical reference solutions for seismic wave propagation (e.g., Uphoff and Bader, 2016; Wolf et al., 2020). Fast time to solution is achieved thanks to end-to-end optimization (Breuer et al., 2014; Heinecke et al., 2014; Rettenberger et al., 2016), including an efficient local time-stepping algorithm (Breuer et al., 2016, Uphoff et al., 2017). This efficient algorithm on high-performance computing architecture provides up to ten-fold speed up (Uphoff et al., 2017).

1268 SeisSol allows accounting for off-fault yielding. Inelastic energy dissipation influences
1269 rupture dynamics such as rupture speed and rupture style (e.g., Gabriel et al., 2013). Off-fault
1270 plasticity is incorporated using the off-line code generator to compute matrix operations in an
1271 efficient way (Wollherr et al., 2018). SeisSol also supports visco-elastic rheologies, using an off-
1272 line code generator similar to that off-fault plasticity. In this study, we use a spatiotemporal
1273 discretization of polynomial degree $p = 4$ $(O5)$ for all simulations.
1274
1275 **A3.2 Mesh generation**
1276 The simulation domain and fault plane geometry model are created using third-party software
1277 GoCad (Emerson paradigm holding, 2018) in a Cartesian coordinate system. We discretize the
1278 unstructured tetrahedral mesh using the meshing software Simmodeler (Simmetrix Inc., 2017).
1279 The mesh element edge length size to 50 m close to the fault plane and 200 m at the surface
1280 topography, yielding a 4 million volume cell mesh. The mesh size on the fault plane is examined
1281 prior to the simulation by calculating the cohesive zone (or process zone) to ensure convergence.
1282 Wollherr et al. (2018, 2019) provide a way to resolve the cohesive zone for the case of SeisSol. To
1283 save the computational costs and at the same time avoid reflection from the domain boundary, we
1284 gradually increase the edge length size of the tetrahedral element by a factor of 6% away from the
1285 fault plane and surface topography. Figure 3 depicts the unstructured tetrahedral mesh used in this
1286 study, overlain by a snapshot of the absolute velocity field at simulation time 5 s, for our preferred
1287 dynamic rupture model (Model 2F), highlighting the effect of the topography on the near-field
1288 ground motions.
1289 The locally refined mesh and high-order spatiotemporal discretization allow capturing the
1290 high-frequency content of the waveforms with high accuracy (little numerical dispersion),

especially in the near-fault region. We estimate the maximum resolved frequency is up to 4 Hz within 7 km distance from the fault zone, and around 1 Hz at 30 km distance from the fault. Simulating 5 s typically requires 15 minutes (average run-time) on Intel Haswell cores with 128 nodes using supercomputer Cray XC40 Shaheen-II, King Abdullah University of Science and Technology, Saudi Arabia.

**Electronic supplement to**

# Dynamic fault interaction during a fluid-injection induced earthquake: The 2017 Mw 5.5 Pohang event

By K. H. Palgunadi, A.-A Gabriel, T. Ulrich, J. A. Lopéz-Comino, P. M. Mai



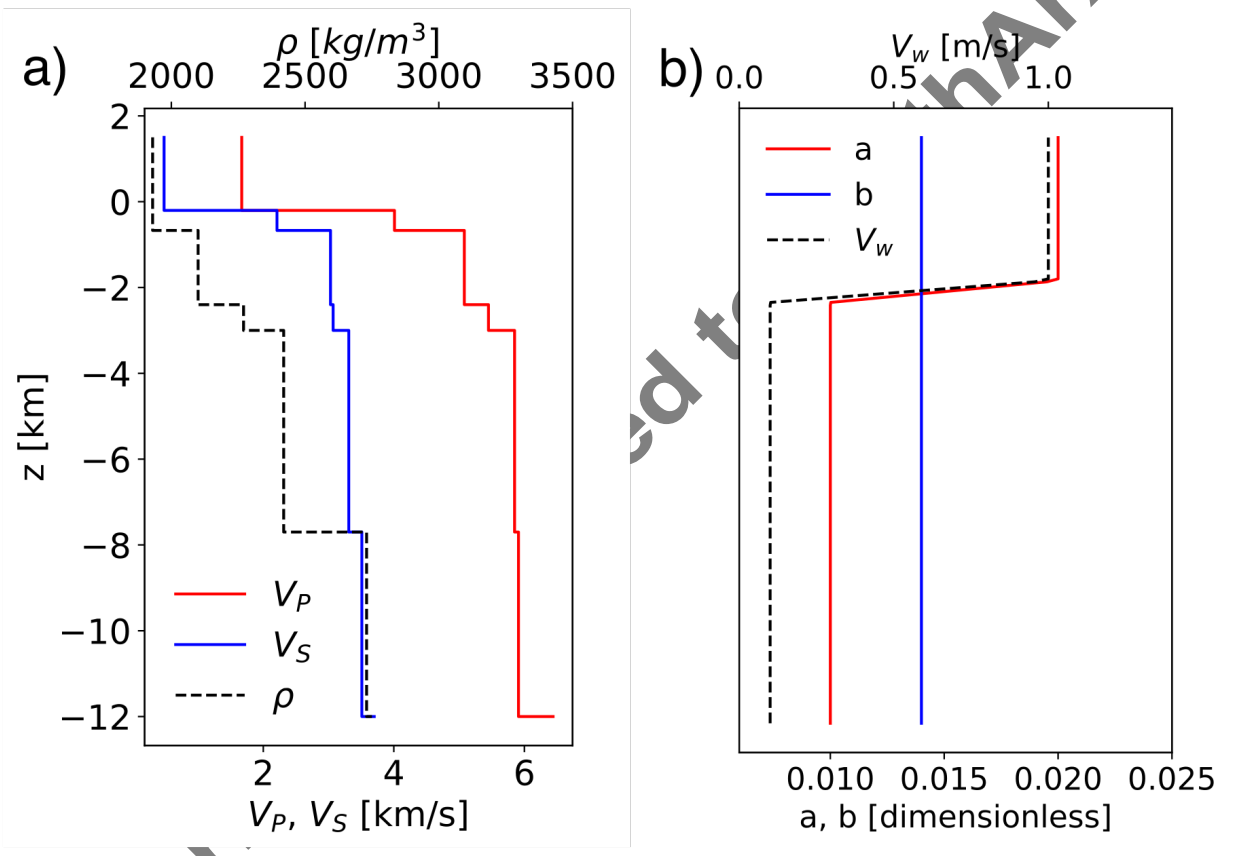


**Figure S1.** Vertical profiles of a) the 1-D model of seismic wave speeds by Woo et al. (2019) and by Korean Government Commission (2019). Panel b) displays the depth-dependent parameters of the velocity weakening rate-and-state friction law.

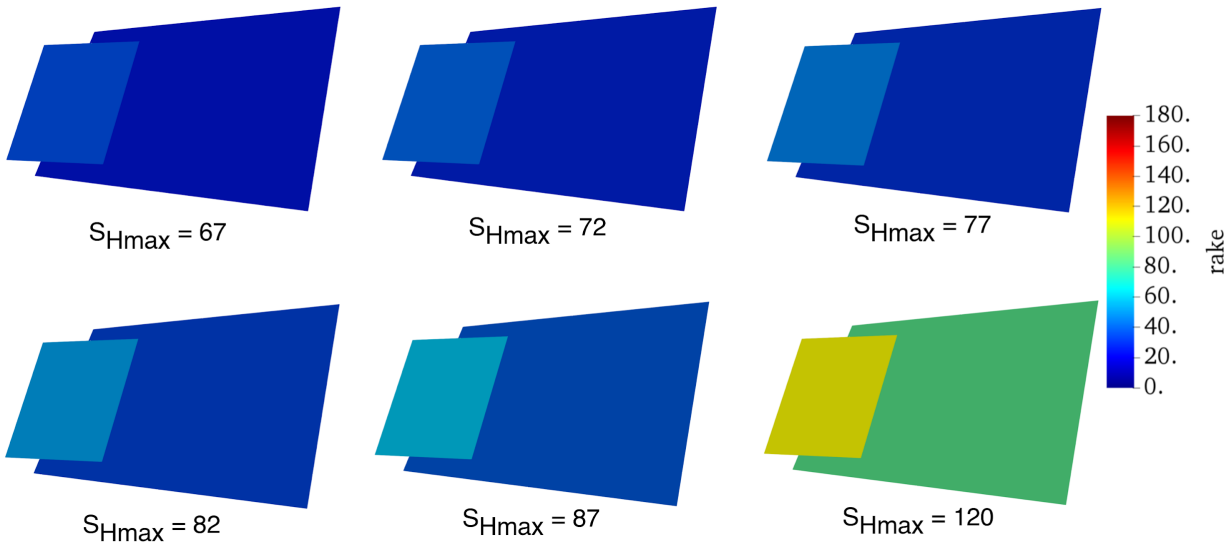


**Figure S2**. Rake of initial (at t=0) shear traction for exemplary orientations of maximum horizontal stress $S_{Hmax}$ (see also Table S1). Thrust-faulting is favoured for $S_{Hmax}$=120°. Note that $S_{Hmax}$=77° corresponds to the findings of Ellsworth et al. (2019).

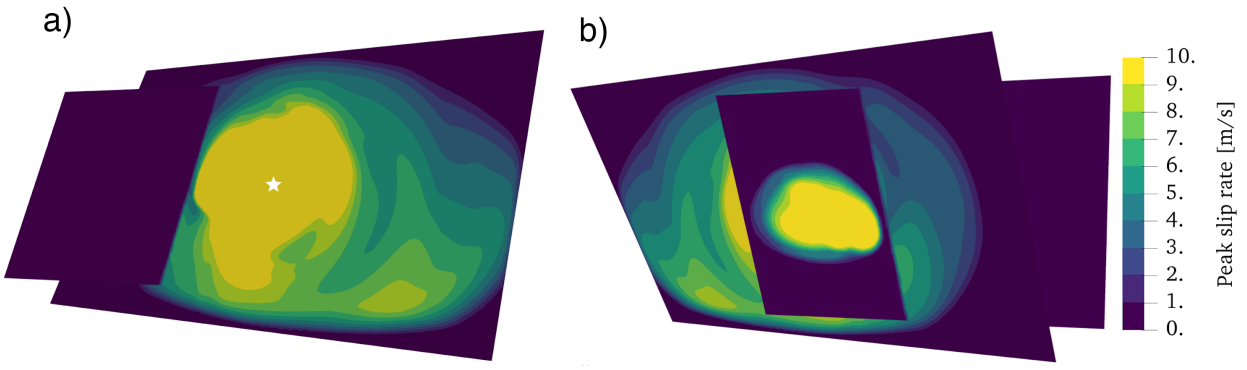


**Figure S3**. Peak slip-rate of the Model 2F. The maximum peak slip rate (saturated yellow color) outside the nucleation zone is 15 m/s. View from a) North and b) South.

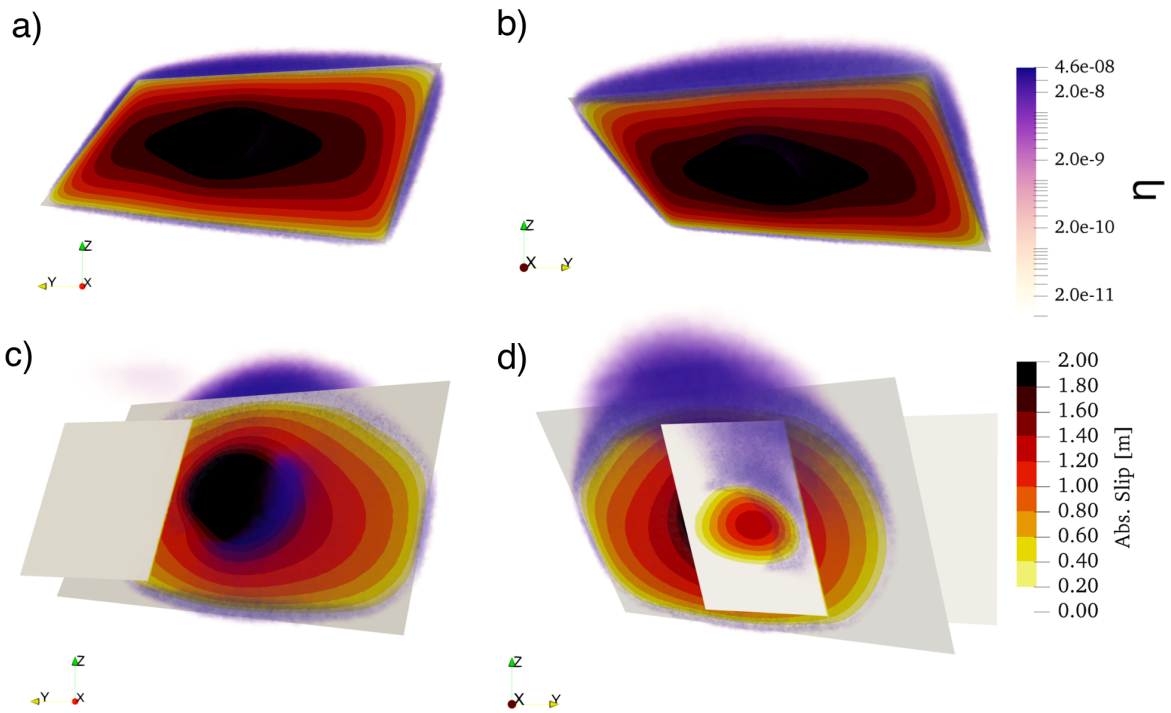


**Figure S4.** Asymmetric off-fault plastic deformation for Model 1F (a and b) and for Model 2F (c and d). a) and c) view from North b) and d) view from South. The accumulated volumetric plastic strain is mapped into the scalar quantity $\eta$ as noted by the purple colorbar.

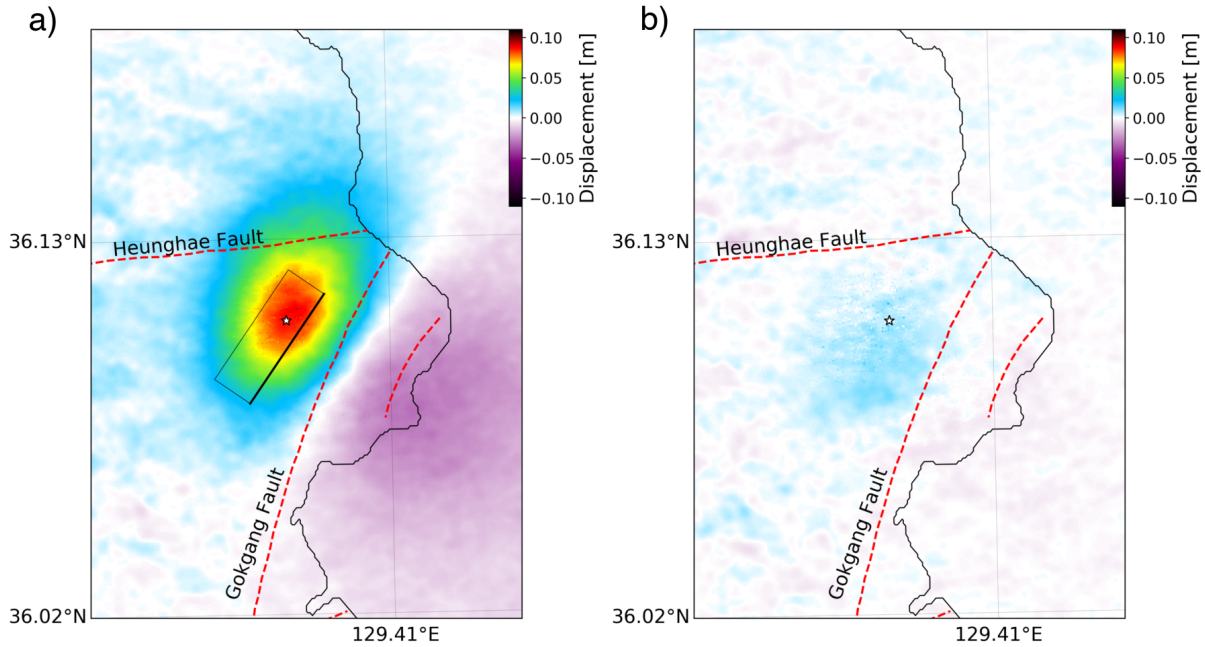


**Figure S5.** Surface displacements. a) Co-seismic surface displacements using only the main fault plane of Model 2F. Rectangle illustrates the fault plane. b) Residual of Model 2F with respect to Model 2F by using only the main fault plane. The dashed red lines represent the traces of the interpreted faults near the EGS site. The white star represents the epicenter of the Pohang earthquake.

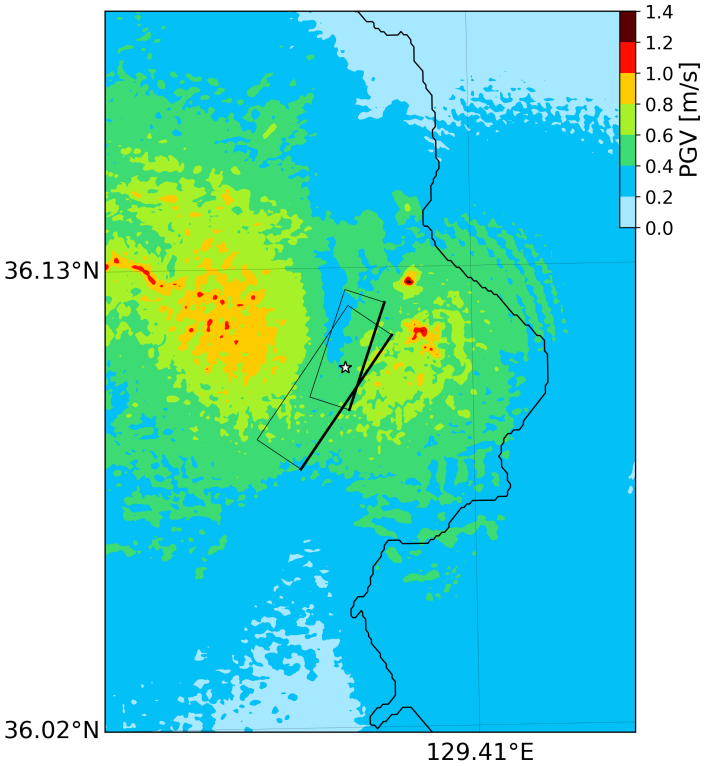


**Figure S6.** Peak ground velocity shake-map (in m/s, based on GMRotD50 (Boore et al., 2006)) for preferred scenario Model 2F, color-contoured 0.2 increments. The white star denotes the epicenter of the Pohang earthquake.

**Table S1. Rake of initial shear traction on the faults of Model 2F**

| $S_{Hmax}$ | Main fault rake (°) | Secondary fault rake (°) |
|---|---|---|
| 52 | 0 | 12 |
| 57 | 3 | 16 |
| 62 | 7 | 20 |
| 67 | 11 | 24 |
| 72 | 15 | 29 |
| 77 | 19 | 35 |

| | | |
|---|---|---|
| 82 | 23 | 41 |
| 87 | 28 | 48 |
| 92 | 34 | 57 |
| 97 | 40 | 66 |
| 102 | 47 | 77 |
| 107 | 55 | 88 |
| 112 | 64 | 100 |
| 120 | 80 | 110 |
| 125 | 91 | 130 |
| 130 | 110 | 140 |
| 135 | 115 | 130 |
| 140 | 120 | 150 |

**Movie M1**: Slip-rate of Model 2F.

(link: https://drive.google.com/open?id=1nm3HZ_YOD-j8t_YatTFfs9prVKplEExj)

## Reference:

Boore, D. M., J. Watson-Lamprey, and N. A. Abrahamson, 2006, Orientation-Independent Measures of Ground Motion, Bull. Seismol. Soc. Am., 96, no. 4A, 1502–1511, doi: 10.1785/0120050209.